UNIVERSITY OF TROMSØ UIT

FACULTY OF SCIENCE AND TECHNOLOGY
DEPARTMENT OF PHYSICS AND TECHNOLOGY

Ultrasound sensor for biomedical applications

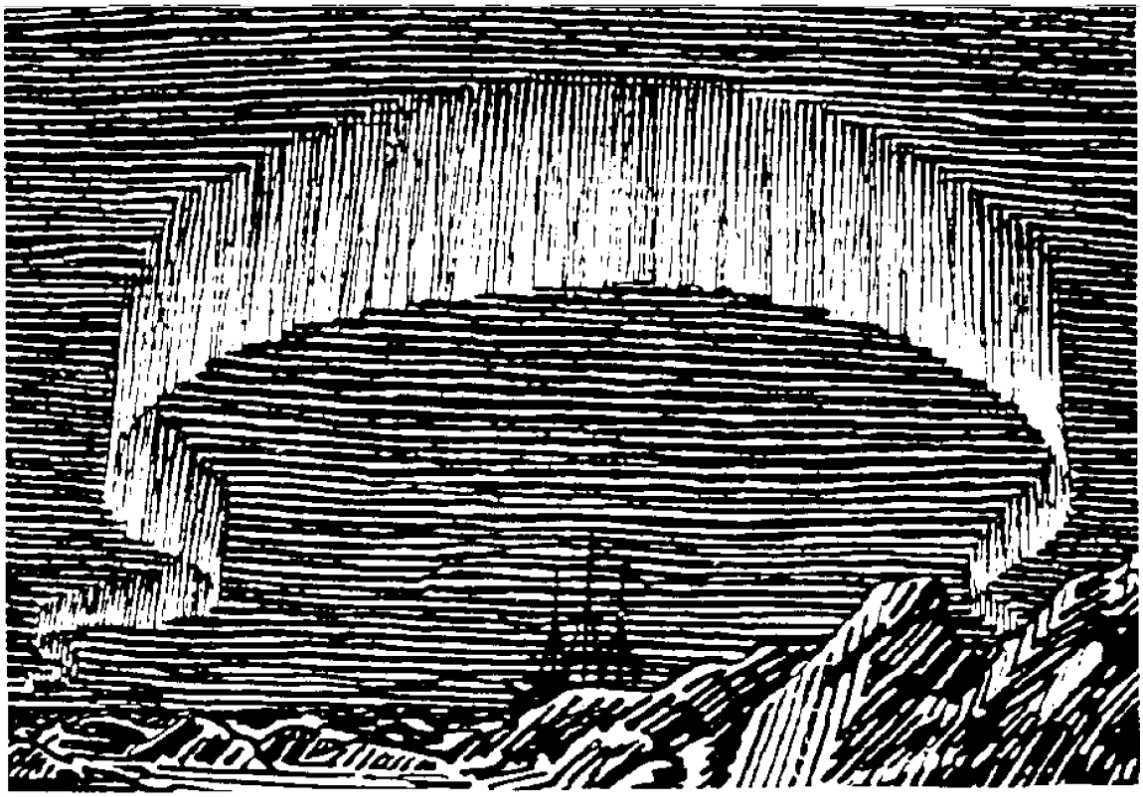

Original by F. Nansen

Helge Øberg

FYS-3921 Master's thesis in electrical engineering

December 2011

Ultrasound sensor for biomedical applications

Abstract

Vesicoureteral reflux (VUR) is an abnormality that causes urine to flow back from the bladder to the kidneys, which may cause renal scarring and kidney damage. A non-ionizing and non-invasive VUR diagnostic technique, based on microwave hyperthermia, is under development. The possibility for improved hyperthermia efficiency and patient safety through implementation of ultrasound transducers is the motivation behind this thesis. The transducers are intended to measure the thickness of the water bolus, which is a cooling devise placed on the patient to avoid skin damage during the heating process.

The main focus of this thesis is on Polyvinylidene fluoride (PVDF) films, which are thin ultrasonic transducers. Basic principles of ultrasound theory and the current microwave antenna are presented. Pressure wave theory and experimental results show that the size and shape of these transducers influence both the transmitted pressure field and the received pulse detectability. Reducing the size of the transducer gives shorter near-field and increased beam width, but these positive properties comes with a trade-off as a smaller size also reduces the sent/received acoustic power. Rectangular transducers are considered for array configurations with transducers dedicated to transmitting or receiving pulses, where the effect of decreased beam spread at corners are negligible. When a transducer operates as both transmitter and receiver, a circular shape is preferable as it is more robust with regard to variations of the angle between the antenna and bolus/skin interface.

The results from experimental work shows that a circular transducer with diameter 2.5 mm fulfills the requirements on beam width, near field length and pulse detectability. Array configuration can not be used as the required beam width is not achievable without compromising pulse detectability. We propose placing three of these circular transducers at the corners of the antenna PCB to reduce their influence on the microwave radiometric measurements. The acoustical backing offered by the microwave antenna is adequate, and the accuracy in the thickness measurements are expected to be < 0.1 mm with the applied detection method.

Acknowledgements

I would first of all like to thank my supervisor, Yngve Birkelund. You have been a constant motivator and allowed me to tap into your vast knowledge in all theoretical and practical aspects of this thesis. My co-supervisors, Frank Melandsø and Svein Jacobsen, also deserve my gratitude for all their inputs and contributions. It has been a true pleasure working with you.

There are many others who have helped me along the way through encouraging words, interesting discussions and suggesting alternative solutions to problems. In fear of forgetting someone I simply say thanks to all of you. Your contributions, regardless of size, have all been invaluable.

Helge Øberg
Tromsø, December 2011

Contents

Chapter 1

Introduction

This thesis is a study of ultrasound used for distance measurement in medical applications where microwave heating is applied. Ultrasound imaging is a well known medical use of acoustics, and the field of acoustics in general has been a subject of research for many years. Although the field is well described, new applications demand continued research. The medical applications in question, uses microwave radiation to heat up tissue in hyperthermia cancer treatment [40] [50] [21], and microwave radiometry to control the temperature of heated urine inside a pediatric bladder for vesicoureteral reflux diagnostics [30] [4] [5] [47] [9]. The latter application will be the main focus of this thesis, but the results will be transferable to the other method.

During the microwave heating process, the skin temperature must be kept down to avoid skin burns and blisters. This is achieved by the use of a water bolus inserted between the radiating antenna and the skin [53] [60]. To estimate how much electromagnetic effect that is actually transmitted into the body, it is crucial to have good knowledge on how much power that is lost in the water due to absorption. This is also important when microwave radiometry is used to measure the heat radiation from the body, as these values are very small. In these calculations, the thickness of the bolus plays a vital role [55] [34]. The focus of this thesis is to investigate how this can be measured by the use of an ultrasonic transducer. Furthermore, it may be possible to measure the thickness of deeper body layers, such as fat and muscle tissue, which the microwaves have to pass to reach the bladder. If this is achieved, the heat power that reached the target can be more accurately approximated.

1.1 Vesicoureteral reflux diagnostic system

Vesicoureteral reflux (VUR) is an abnormality which causes urine to flow backwards from the bladder to the kidneys [30]. Children with VUR are predisposed to urinary tract infections and renal scaring which may lead to kidney damage [6] [35]. The two most common diagnostic imaging techniques are voiding cystourethrography (VCUG) and radionuclide cystography (RNC) [15]. Both techniques expose patients to ionizing radiation, although the latter does so to a smaller extent. The risk of long-term effects due to this exposure and the discomfort associated with bladder catherterization, spur the development of new non-invasive and non-ionizing diagnostic techniques [28] [2] [16] [14] [18]. One approach suggests a passive microwave diagnostic system to detect the reflux of urine from the noninvasively heated bladder flowing into the kidneys by using a radiometer [5]. This system has been subject to further research and the results are promising [30] [1] [4]. Implementation of ultrasound for distance measurements may further aid this progress.

1.2 The VUR diagnostistic set-up

Electromagnetic waves with frequency ranging from 300 MHz to 300 GHz are denoted microwaves. On a molecular level, the non-ionizing microwaves are absorbed and manifested as either vibrational energy or heat [43]. Soft tissue has a large absorption rate, resulting in much energy being deposited near the antenna. In the microwave heating process, the largest heat increase will occur near the skin surface of the patient. Without any form of cooling the required increase in urine temperature can not be achieved without damaging the patient's skin.

A simplified diagram of the complete VUR diagnostic set-up is shown in Figure 1.1, and a cross section of the abdomen, with urine filled bladder, obtained by CT imaging is shown in Figure 1.2.

The microwave antenna used is printed upon a printable circuit board (PCB) which is placed on the surface of the water bolus. The optimal position for a ultrasound transducer to accurately measure the thickness of the water bolus for energy loss calculations, is at the center of the microwave antenna. Since there might be small variations in the thickness of the water bolus, measuring thickness directly below the microwave antenna should give the most accurate result. Minimizing the effects on the antenna characteristics is desirable, rendering a PVDF (Polyvinylidene Fluoride) transducer with its small size and flexibility, as a good candidate to place at the center of the antenna [10].

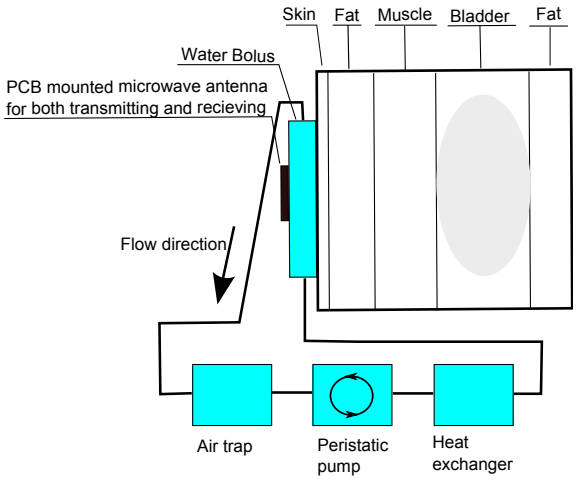

Figure 1.1: Simplified model of complete VUR diagnostic system. Surrounding microwave circuits left out

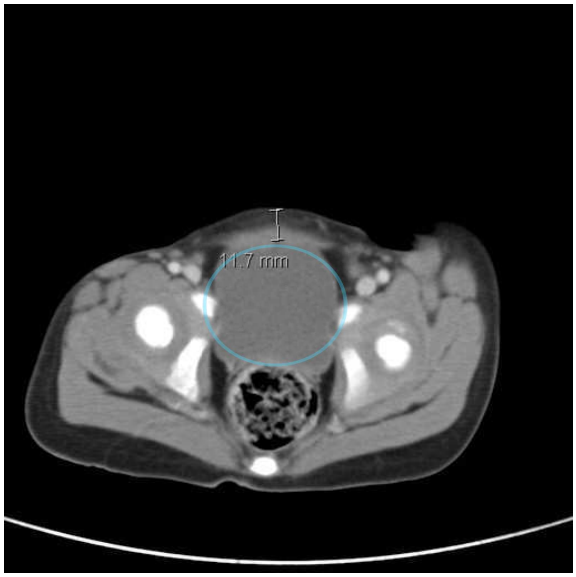

Figure 1.2: CT image showing the approximate depth of the bladder (circled). The depth found in this image was 11.7 mm.

1.3 Water bolus

As previously mentioned, the technique used to cool the skin during the heating process involves a water bolus, the design of which is crucial to achieve homogeneous cooling [56] [33]. The water bolus used in this thesis is rectangularly shaped and made of medical-grade polyvinyl chloride (PVC) film. In addition to containing water, the water bolus has open cell filter foam placed inside it for structural support. The original design includes one inlet and outlet pair. However, experiments and simulations conducted at the University of Tromsø indicate that this results in uneven cooling of the skin, which has given rise to a new design with two outlets and inlets [60]. The water bolus used in this thesis is shown in Figure 1.3.

Figure 1.3: Water bolus used in this project. The black areas are open cell filter foam with two different thicknesses.

The complete cooling system is a closed loop comprised of an air trap, a peristaltic pump, the bolus it self and a heat exchanger for cooling (see Figure 1.1). The use of a closed loop system makes the thickness of the bolus more stable during the heating process, as the water pressure inside is kept nearly constant. Air bubbles inside the bolus, which affects both the microwaves and ultrasonic waves, are effectively captured in the air trap.

1.4 Project structure

In chapter 2, *Ultrasonic Theory*, properties of acoustic wave propagation and ultrasonic transducers, will be explained. An introduction to the microwave heating system is presented in chapter 3. In chapter 4, signal processing, transducer design aspects and the experimental methodology are presented. All experimental results are displayed and compared in chapter 5, and a discussion of these findings are presented in chapter 6. A conclusion, together with suggestions for further work, can be found in chapter 7.

Chapter 2

Ultrasonic theory

2.1 Acoustic wave propagation

The complete theory on which this section is based on can be found in the books *Principles of Measurement Systems*, *Fundamentals and Applications of Ultrasonic waves* and *Ultrasonic Testing* [8] [22] and [59]. A wave is a disturbance that conveys energy as a function of both time and position. Sound is a pressure wave which implies the need of a medium to propagate in. Ultrasound refers to those sound waves with frequencies above the range of the human ear and below the range of hypersound i.e. frequencies higher than 18 kHz and lower than 1 GHz as shown in Figure 2.1 [22] . Acoustic wave properties are the same throughout the whole frequency spectrum, except in the extreme limits. Therefore we do not have to look at ultrasound in particular when deriving the wave equation.

As a starting point, we just constitute that an idealization of many types of wave motion can be expressed mathematically in what is know as the wave equation

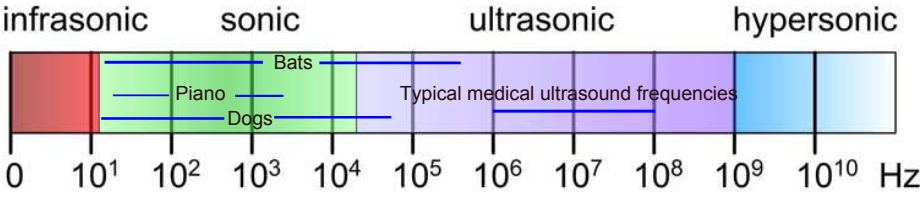

Figure 2.1: The acoustic frequency spectrum.

$$c^2\nabla^2 u(x,y,z,t) - \frac{d^2u}{dt^2} = 0. \tag{2.1}$$

Here u is the physical property associated with the wave, c is the speed and the Laplace operator, ∇^2, is defined by

$$\nabla^2() = \frac{\partial^2}{\partial x}() + \frac{\partial^2}{\partial y}() + \frac{\partial^2}{\partial z}(). \tag{2.2}$$

Although it is common to picture a sinusoidal waveform, it can be shown that any waveform satisfies the solution to equation (2.1) as long as it is a function of type $u = f(x \pm ct)$. The sign indicates which direction the wave travels. To arrive at the wave equation for sound waves we will first take care of the simplest case, the 1-D lossless acoustic wave, before working our way towards a more complete expression. For this case, we only need to consider conservation of mass, conservation of momentum and the equation of state for fluids. When taking loss into account we also need to look at conservation of energy.

2.1.1 Conservation of mass

Consider a compressible fluid flowing through a duct with arbitrary, constant cross section with surface area S, as shown in Figure 2.2. Define a small section between x and $x+\Delta x$ as an infinitesimal control volume (CV). The point being to look at the rate of change of mass inside the CV.

First we make two assumptions

- The CV is fixed in space
- The flow is one-dimensional

The second assumption leads to both the particle velocity, u, and density, ρ being constant over a cross section of the tube. The mass flow of the fluid is represented

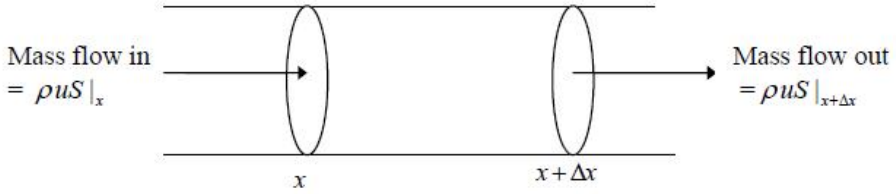

Figure 2.2: Control volume for conservation of mass [11].

by the quantity ρuS, which has unit mass per unit time. Mathematically the conservation of mass inside the CV can be expressed as

$$\frac{\partial}{\partial t}(S\rho\Delta x) = \rho uS|_x - \rho uS|_{x+\Delta x}. \tag{2.3}$$

Where ρ is the average density in the control volume and u is the average mass flow speed. By rearranging equation (2.3), and letting $\Delta x \to 0$, it can be shown that

$$\frac{\partial \rho}{\partial t} + u\frac{\partial \rho}{\partial x} + \rho\frac{\partial u}{\partial x} = 0, \tag{2.4}$$

which is the equation of continuity for conservation of mass.

2.1.2 Conservation of momentum

We still use the same control volume as in the previous section.

The momentum per unit volume is given by ρu and the momentum flux by $\rho u^2 S$, which has units momentum per unit area per unit time.

Now let us expand the list found in section 2.1.1 with two additional assumptions

- Body forces, such as gravity, is not important.
- The fluid is inviscid. This means that the only significant force acting on the surface of the control volume is due to the pressure.

These assumptions imply that the only forces acting on the control volume are $PS|_x$ and $PS|_{x+\Delta x}$. Here P is the sum of the acoustic and ambient pressure on the surface S. Newtons law can now be written as

$$\begin{aligned} \frac{\partial}{\partial t}(\rho uS\Delta x) &= \rho u^2 S|_x - \rho u^2 S|_{x+\Delta x} + PS|_x - PS|_{x+\Delta x} \\ \frac{\partial}{\partial t}(\rho u) &= -\frac{\rho u^2|_{x+\Delta x} - \rho u^2|_x}{\Delta x} - \frac{P|_{x+\Delta x} - P|_x}{\Delta x} \end{aligned} \tag{2.5}$$

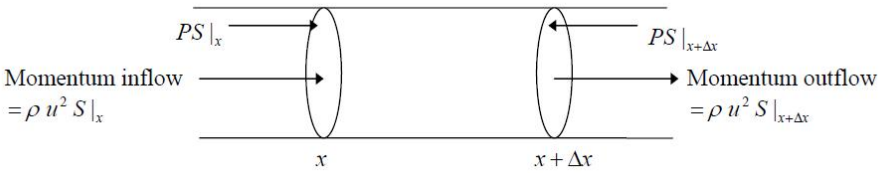

Figure 2.3: Control volume for conservation of momentum [11].

We can express Newtons second law with account taken to the momentum inflow across the boundaries of the control volume with words as:

"Time rate of increase of momentum inside CV = New momentum inflow across boundaries + sum of the forces acting on the CV."

If we let $\Delta x \to 0$ in equation (2.5) and rearranging, we end up with the expression

$$\frac{\partial \rho u}{\partial t} + \frac{\partial \rho u^2}{\partial x} + \frac{\partial P}{\partial x} = 0, \tag{2.6}$$

which is the momentum equation.

2.1.3 Equation of state

An arbitrary equation of state is a expression linking thermodynamic variables. In acoustics we can utilize the equation of state linking pressure, density and entropy

$$P = P(s, \rho). \tag{2.7}$$

The variable s in the entropy per unit mass. If the fluid is lossless the entropy remains constant. Therefore the fifth and last assumption is added to the assumption list.

- The flow is lossless.

This assumption leads to the equation of state only being dependent on density.

$$P = P(\rho) \tag{2.8}$$

For a arbitrary fluid, either gas or liquid, the general isentropic equation of state can be expressed by a Taylor expansion of the condensation given by $(\rho - \rho_0)/\rho_0$.

$$P = p_0 + A\frac{\rho - \rho_0}{\rho_0} + \frac{B}{2!}\left(\frac{\rho - \rho_0}{\rho_0}\right)^2 + \frac{C}{3!}\left(\frac{\rho - \rho_0}{\rho_0}\right)^3 + \cdots \tag{2.9}$$

Here the coefficients are determined through experiments or by other means. In most cases the condensation is very small leading to A being of most importance. To simplify the equation of state found in equation (2.9), we can introduce sound speed, defined as

$$c^2 \equiv \left.\frac{\partial P}{\partial \rho}\right|_{s=constant} = \frac{dP}{d\rho}. \tag{2.10}$$

When there is no condensation ($\rho \to \rho_0$) the sound speed becomes a constant, denoted by c_0^2. Furthermore, by defining the acoustic pressure as $p \equiv P - p_0$ and the excess density as $\delta\rho \equiv \rho - \rho_0$, we can from equation (2.9) arrive at the isentropic equation of state

$$p = c_0^2 \delta\rho \left(1 + \frac{B}{2!A}\frac{\delta\rho}{\rho_0} + \frac{C}{3!A}\left(\frac{\delta\rho}{\rho_0}\right)^2 + \cdots\right). \tag{2.11}$$

2.1.4 Resulting wave equation

Here we will combine the results of the previous sections to arrive at the wave equation for a lossless homogeneous fluid. The equations (2.4), (2.6) and (2.11) are all non-linear, but can be linearized by using a small-signal approximation. This approximation is widely used in acoustics and is valid for louder sounds than what most humans ever encounter. We assume the fluid is quiet when no acoustic waves are present. This means that the pressure, density and particle velocity are $P = p_0$, $\rho = \rho_0$ and $u = 0$, respectively. The basic assumption is that the disturbance caused by a acoustic wave are much smaller than the static quantities of same dimensions. We start with the excess density

$$|\delta\rho| << \rho_0. \tag{2.12}$$

Given that this assumption is valid we can identify from equation (2.11) that the acoustic pressure must obey the following inequality

$$|p| << \rho_0 c_0^2, \tag{2.13}$$

and in a similar fashion it can be shown that [11]

$$|u| << c_0. \tag{2.14}$$

By first linearizing the equation of state, the conservation of mass equation and the conservation of momentum equation, and then combining them, we arrive at the wave equation given by [11]

$$\underline{c_0^2 \frac{\partial^2 u}{\partial x^2} - \frac{\partial^2 u}{\partial t^2} = 0.} \tag{2.15}$$

A standard solution of the wave equation can be written on the form

$$p(x,t) = Ae^{j(\omega t - kx)}, \tag{2.16}$$

where A is the amplitude, ω is the angular frequency and k the wave number.

2.2 Impedance

Impedance can loosely be explained as the resistance a medium imposes on a propagating effect. If we use electricity as an analogue, impedance is the resistance a circuit imposes on the flow of current through it when a given voltage is impressed a cross the circuits terminals. Here voltage can be viewed as a *push* variable and current as a *flow* variable. The impedance is given by the ratio of voltage to current. From this we can infer that impedance may be interpreted as a ratio of a push variable to a corresponding flow variable [11]. It is from this possible to conclude that that the acoustic impedance must be the ratio of pressure to either sound or particle speed. To find the acoustic impedance we can start with the general solution of the wave equation for an forward propagating wave, discussed in the beginning of this chapter, interpreted

$$u = f(x - c_0 t). \tag{2.17}$$

Using the linearized momentum equation, which is written as

$$\rho_0 \frac{\partial u}{\partial t} + \frac{\partial p}{\partial x} = 0, \tag{2.18}$$

we find that

$$\frac{\partial p}{\partial x} = -\rho_0 \frac{\partial u}{\partial t} = \rho_0 c_0 f'(x - c_0 t), \tag{2.19}$$

and by integrating this equation we find that

$$p = \rho_0 c_0 f(x - c_0 t) = \rho_0 c_0 u. \tag{2.20}$$

Now, we can define the characteristic impedance as

$$Z_0 \equiv \left(\frac{p}{u}\right)_{outgoing} = \rho_0 c_0, \tag{2.21}$$

which gives us three different useful impedances in acoustics. The *acoustic impedance* is the ratio of average sound pressure over the surface to the volume velocity q of the fluid through the surface

$$Z_{ac} = \frac{p_{av}}{q}. \tag{2.22}$$

The *specific acoustic impedance* is the ratio of pressure at a point to the particle velocity at that point

$$Z_{acsp} = \frac{p}{u}. \tag{2.23}$$

The *mechanical impedance* is the ratio of the force acting on a specified area to the particle velocity through that area

$$Z_{mech} = \frac{f}{u}. \tag{2.24}$$

The most commonly used impedance of the three is the specific acoustic impedance [11].

2.3 Ultrasonic waves at an interface

Two liquids, I and II, share a common boundary at position $x = 0$. If an acoustic wave, p_i, traveling in liquid I hits the boundary between the liquids perpendicularly, a transmitted and reflected wave, p_t and p_r respectively, will be generated, as shown in Figure 2.4. To determine the magnitude of the reflected and transmitted wave we have to look at the boundary conditions. They must ensure continuity of pressure and velocity, which can be formulated as:

1. Acoustic pressure must be equal on both sides of the interface. This is essentially a result from Newtons third law.
2. The normal component of the particle velocity must be equal on both sides.

The three waves can be represented as

$$\begin{aligned} p(x,t)_i &= Ae^{j(\omega t - k_1 x)} \\ p(x,t)_r &= AR_p e^{j(\omega t + k_1 x)} \\ p(x,t)_t &= AT_p e^{j(\omega t - k_2 x)}. \end{aligned} \tag{2.25}$$

From boundary condition one, we see that

$$\begin{aligned} p_i(0,t) + p_r(0,t) &= p_t(0,t) \\ 1 + R_p &= T_p. \end{aligned} \tag{2.26}$$

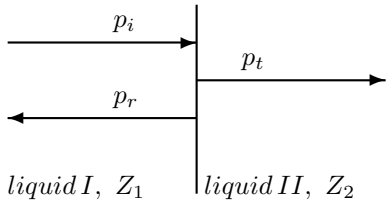

Figure 2.4: Incident, reflected and transmitted wave at normal incident. Boundary at $x = 0$

The particle velocity can be found from the definition of characteristic impedance given in equation 2.23

$$\begin{aligned} u_i(0,t) + u_r(0,t) &= u_t(0,t) \\ \Rightarrow \frac{p_i(0,t)}{Z_1} - \frac{p_r(0,t)}{Z_1} &= \frac{p_t(0,t)}{Z_2} \\ \Rightarrow \frac{1}{Z_1}(1 - R_p) &= \frac{T_p}{Z_2}. \end{aligned} \tag{2.27}$$

Solving with respect to the transmission and reflection coefficient gives

$$\begin{aligned} T_p &= \frac{2Z_2}{Z_1 + Z_2} \\ R_p &= \frac{Z_2 - Z_1}{Z_1 + Z_2}. \end{aligned} \tag{2.28}$$

From these results we can also show that the law of conservation of energy is satisfied. The acoustic intensity is defined as

$$I \equiv \frac{p^2}{2Z}. \tag{2.29}$$

At the boundary ($x = 0$) we get

$$\begin{aligned} \frac{I_t}{I_i} &= \frac{Z_1}{Z_2}|T_p|^2 \\ \frac{I_r}{I_i} &= |R_p|^2. \end{aligned} \tag{2.30}$$

Thus, it can be shown that

$$I_i = I_t + I_r, \tag{2.31}$$

which is the law of conservation of energy.

2.4 Loss and distortion

In acoustics there are many different phenomena leading to loss in strength and distortion of signals between transmitter and receiver. These phenomena include, in short, reflection and transmission at boundaries between media, attenuation in the media and loss in received energy due to dispersion. Dispersion is basically that the phase velocity of a wave is frequency dependent in some media. In other words; a broad-banded signal sent through a dispersive media will be distorted. The scale of e.g. acoustic waveguides, films, etc., can also lead to this phenomena. Such components are not used in our medical application. Furthermore, the dispersion in water and soft tissue is relatively low [22] [17]. Therefore, this topic will not be taken further here. Loss associated with interfaces is a loss of *received* acoustic energy, rather than a loss in *total* acoustic energy. In single mode thickness measurements, some of the energy is reflected and some transmitted. The received signal, reflected from the interface has therefore less energy. In multilayer detection this becomes even more crucial, as the wave transmitted through the first layer is the incident wave on the second and so forth. There is an exception where interfaces actually cause a loss in total acoustic energy; when an acoustic wave travels along an interface. This is basically due to that parts of the wave are in different media at the same time. Since we will assume nearly perpendicular incident waves in this thesis, this topic will also not be discussed further. A more in dept explanation on this phenomena can be found in David T. Blackstock's book *Fundamentals of physical acoustics* [11].

2.4.1 Attenuation

The notion of attenuation refers to the absorption of acoustic energy in the medium which conducts the wave. There are several different effects that contribute to the total loss of energy. The so-called classic attenuation is the loss due to viscosity and thermal conductivity, but also molecular processes which transforms acoustic energy into internal molecular energy occurs. In general, all loss effects inside a medium can be described by a phase difference between acoustic pressure and the medium response [22]. Lets define the displacement u of a wave as $u = u_0 \exp j(\omega t - kx)$, where k is the wave number. Attenuation is normally incorporated by a complex wave number, so that $k = \beta - j\alpha$. Here α is the attenuation constant. The displacement is then

$$u = u_0 \exp j(\omega t - \beta x) \exp(-\alpha x) \tag{2.32}$$

To measure the attenuation you can introduce a amplitude ratio r_{12} of a wave at two different positions x_1 and x_2. This leads to the expression,

$$r_{12} = e^{\alpha(x_2 - x_1)} \tag{2.33}$$

Solved for α, the attenuation coefficient in dB/m is

$$\alpha(dB/m) = 8.686 \frac{\ln(r_{12})}{x_2 - x_1} (Np/m) \tag{2.34}$$

Although this gives a practical way of measuring the overall attenuation, we still have not looked at the physical reasons why it occurs. These reasons are described in the rest of this section.

A solution of the wave equation for the displacement $u(x,t)$ gives rise to a relationship between pressure and relative density change or condensation

$$p = -\rho_0 v_0^2 \frac{\partial u}{\partial x} = \rho_0 v_0^2 s, \tag{2.35}$$

where ρ_0 is the density at equilibrium pressure, v_0 is the bulk velocity of the wave and $s = -S$ is the relative density change and $S = \frac{\partial u}{\partial x}$ is the dilatation. By adding a term due to viscosity, the expression in 2.35 becomes [22]

$$p = \rho_0 v_0^2 s + \eta \frac{\partial s}{\partial t}, \tag{2.36}$$

where η is a viscosity coefficient. If a pressure change in form of a step function, it can be shown that

$$s = \frac{\Delta p_0}{\rho_0 v_0^2} \left(1 - \exp\left(-\frac{\rho_0 v_0^2 t}{\eta}\right)\right) \tag{2.37}$$

where Δp_0 is the pressure applied at $t = 0$. When the pressure is removed

$$s = \frac{\Delta p_0}{\rho_0 v_0^2} \exp\left(-\frac{\rho_0 v_0^2 t}{\eta}\right) \tag{2.38}$$

As an analogue to an electrical L-R circuit with relaxation time $\tau = L/R$, we can identify a viscous relaxation time as

$$\tau = \frac{\eta}{\rho_0 v_0^2}. \tag{2.39}$$

Lets now turn our attention to the attenuation caused by the viscosity of a fluid. Assuming the wave displacement, $u(x,t)$, is still given by equation (2.32). Using the Stokes' term for the pressure leads to the wave equation taking the form

$$\frac{\partial^2 u}{\partial t^2} = v_0^2 \frac{\partial^2 u}{\partial x^2} + \frac{\eta}{\rho_0} \frac{\partial^2 u}{\partial x \partial \tau}. \tag{2.40}$$

By inserting (2.32) into (2.40) and separating into real and imaginary parts, yields the expression for the attenuation

$$\alpha^2 = \frac{\omega^2}{2v_0^2 \left(\frac{1}{\sqrt{1+\omega^2\tau^2}} - \frac{1}{1+\omega^2\tau^2} \right)}. \tag{2.41}$$

For most fluids at room temperature we have that $\omega\tau << 1$ in the ultrasonic frequency range, which leads to [22]

$$\alpha \, \frac{\omega^2 \tau}{2v_0} = \frac{\omega^2 \eta}{2\rho_0 v_0^3}. \tag{2.42}$$

This result shows that the attenuation coefficient is proportional to the frequency squared, hence increasing the frequency leads to a rise in attenuation. The phase velocity will also be modified, but this change is small and can in most cases be neglected.

As an acoustic wave travels through a liquid, some areas will be compressed and others expanded leading to spatial pressure differences. If the process is unadiabatic, which means that the thermal conductivity $k \neq 0$, heat will flow from the compressed to the expanded regions. Similarly to the effect of viscosity, the heat transfer will lag, or be slower than, the applied pressure. This leads to additional attenuation due to the thermal conduction. As for the attenuation caused by viscosity, a relaxation time, τ_{th}, can be expressed as

$$\tau_{th} = \frac{k}{\rho_0 v_0 C_p}, \tag{2.43}$$

where k is the thermal conductivity and C_p is the specific heat capacity at constant pressure. When applying the assumption $\omega\tau << 1$ and adding the resulting attenuation approximation to the viscosity term given in equation (2.42), the result is the expression for the so-called classical attenuation coefficient of liquids

$$\alpha = \frac{\omega^2}{2\rho_0 v_0^3} \left(\frac{4\eta}{3} + \frac{k(\gamma - 1)}{C_p} \right) \tag{2.44}$$

where γ is the adiabatic index. When the viscosity term dominates the attenuation, or the liquid is inert, the classic expression just stated is in very good agreement with experiments. In other cases, experimentally acquired attenuation values are much higher then what the expression indicates.

This is because of a phenomena called molecular relaxation. To look into this I will give a brief physical description. An ultrasonic wave enters a physical system at constant temperature. This results in the system becoming exited to a higher energy state by absorption. To return to equilibrium the system has to release energy to the surroundings, the rate of which is given by a temperature dependent relaxation time. If the ultrasonic wave has a low frequency in the range $\omega\tau << 1$, this effect is almost reversible and the attenuation minimal as the system follows the applied field in phase. In the opposite case, where $\omega\tau >> 1$, the frequency is so high that the system can not follow the field at all and almost no energy is absorbed by the system, again resulting in minimal attenuation. As $\omega\tau \rightarrow 1$ the system starts to follow the field and absorbing energy. It is a well defined attenuation peak at $\omega\tau = 1$. This is the reason for the assumption $\omega\tau << 1$, when deriving the classical attenuation coefficient for liquids.

2.5 The ultrasonic transducer

A transducer is a device that converts energy from one form to another, e.g. an antenna converts electrical energy into electromagnetic waves. All transducers can convert energy both ways between two energy forms. Although the properties of sound waves are the same throughout the acoustic spectrum, the way of realizing certain frequency bands can differ (like a speaker in the audible frequency range). There exist several different ways to excite ultrasonic waves, but the piezoelectric effect is the most commonly utilized. A piezoelectric material is a material that has both elastic and electromagnetic properties. Since a piezoelectric material can convert mechanical energy into electrical energy, and vice versa, a single piezoelectric ultrasonic transducer can work both as a receiver and a transmitter. This is referred to as using a transducer in *single mode*, and in this case special care has to be taken to distinguish between when the transducer is transmitting and receiving.

2.5.1 The piezoelectric effect

Piezoelectricity is a phenomenon that occurs in some materials when stress is applied. In addition to the resulting strain, a difference of potential between the opposing sides of the crystal is produced. This is called the direct piezoelectric effect which is used in a microphone to convert sound waves into an electrical signal. Running the piezoelectric transducer in reverse utilize the indirect effect, producing strain when applying a difference in potential. A piezoelectric

crystal is characterized by the absence of a center of symmetry. This is not a sufficient condition as 20 of the total 21 crystals lacking a center of symmetry are piezoelectric [22].

To explain the physics behind the piezoelectric effect we can use the case of quartz as an example [22]. The set-up is composed of two conducting plates which can support stress, placed on opposite sides of the piezoelectric quartz crystal. In the absence of stress the molecular system of positive and negative charges has a net polarization of zero as they share a common center of gravity. When, on the other hand, a compressive or tensile stress is applied, the positive and negative charges have different centers of gravity resulting in a molecular dipole moment. Thus, a net polarization occurs which leads to a build up of charge on the two conductive plates, resulting in a potential difference between them. The sign depends on whether a compression or expansion occurred. If an AC stress is applied, a resulting AC potential difference presents itself at the same frequency and magnitude proportional to that of the applied stress.

If we assume a sufficiently small frequency (*system dimension* << *wavelength*) the electric displacement, D, of a piezoelectric material can be modeled as

$$D(E, S) = \epsilon_0 E + P(E, S) \tag{2.45}$$

where E is electric field, ϵ_0 is permittivity, P is polarization field and $S = \frac{\partial u}{\partial x}$ is elastic strain. Notice that the polarization is a function of both electric field and strain. The polarization between two point charges (-q and +q) is defined as

$$\underline{P} = q\underline{a} = qa\underline{e_a}, \tag{2.46}$$

where $\underline{a}$ is the vector pointing from the negative to the positive point charge. In one dimension, the electrical bindings in the dipole between the positive and negative charge can be illustrated as a spring. If we stretch it out, the spring or electric force acting, wants to restore it to its equilibrium state. With this in mind we can construct a dipole-mechanical model for the piezoelectric effect as shown in Figure 2.5.

In a similar way we can look at the elastic properties for piezoelectric materials, starting with Hook's law for a pure elastic material

$$T = cS \tag{2.47}$$

where T is stress, c is the elastic modulus and S is strain. The earlier discussion implies that the stress in piezoelectric materials has to be dependent on any applied electrical field. This means that

$$T(S, E) = cS(E) \tag{2.48}$$

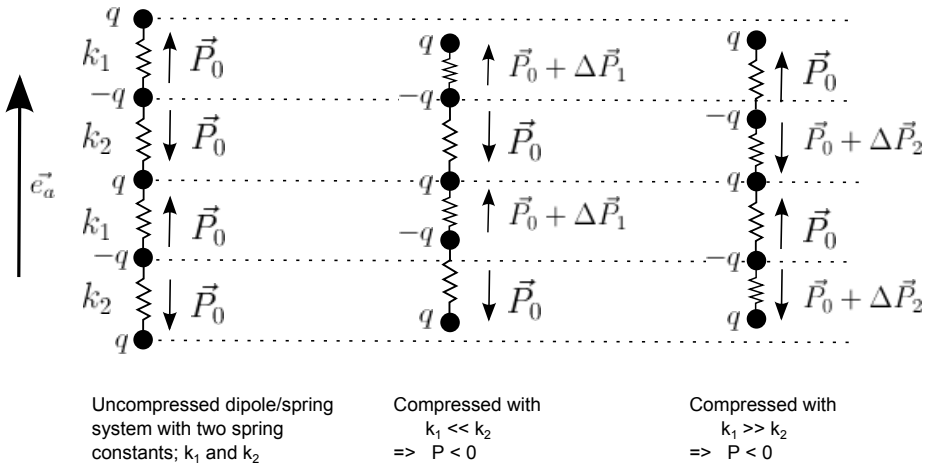

Figure 2.5: Model for the piezoelectric effect. P is the polarization, and ΔP is the piezoelectric contribution to it when the material is compressed.

The effect of an electrical field can again be modeled with a dipole-spring system as shown in Figure 2.6.

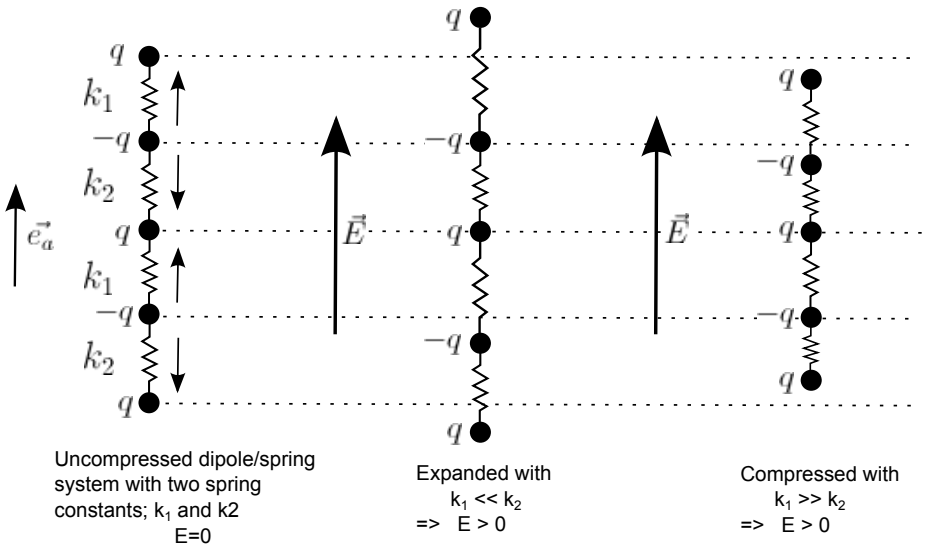

Figure 2.6: The functionality of an applied electric field E on a piezoelectric material

2.5.2 Characterization of transducers

There are several different concepts that need explanation before we can start to look at the different materials and designs used to manufacture an ultrasonic transducer. These concepts include *coupling factor*, *quality factor* and *directionality*.

The coupling factor, K, is used to measure the efficiency of the coupling of electrical to mechanical energy. It can be shown that the displacement in equation (2.45) can be rewritten from linearization through a Taylor expansion as

$$D(E,S) \approx \left(\frac{\partial D}{\partial E}\right)_0 E \left(\frac{\partial D}{\partial S}\right)_0 S = \epsilon^S E + eS, \tag{2.49}$$

where ϵ^S is the permittivity at constant or zero strain and e is the piezoelectric stress constant [22]. The use of superscript to denote *at constant or zero* is standard notation in the literature, and care should be taken to not confuse it with *to the power of*. Linearization of Hook's law in equation (2.48) yields

$$T(S,E) \approx \left(\frac{\partial T}{\partial S}\right)_0 S \left(\frac{\partial T}{\partial E}\right)_0 E = c^E S - eE, \tag{2.50}$$

where c^E is the elastic constant at constant E, and e is the piezoelectric stress constant. In the two last equations, (2.48) and (2.49), we have established a linear relations between the two electromagnetic variables, D and E, and the two mechanical variables, S and T. Other linear relations can be found by solving these equations with respect to the two remaining variables. From equation (2.50)

$$S = \frac{1}{c^E}T + \frac{e}{c^E} = s^E T + dE \tag{2.51}$$

where s^E is the inverse elastic constant and d is the piezoelectric d-constant. By inserting this result into equation (2.49), it can be shown

$$\begin{aligned} D &= \epsilon^S E + e\left(s^E T + dE\right) \\ &= \epsilon^S \left(1 + \frac{e^2}{\epsilon^S c^E}\right) E + dT \\ &= \epsilon^T E + dT, \end{aligned} \tag{2.52}$$

where $\epsilon^T = \epsilon^S \left(1 + \frac{e^2}{\epsilon^S c^E}\right)$ is the permittivity at constant T. The ratio between ϵ^S and ϵ^T is

$$\frac{\epsilon^S}{\epsilon^T} = 1 - \frac{e^2}{\epsilon^T c^E} = 1 - K^2, \tag{2.53}$$

where K is the coupling factor. In a more general form K can be defined as

$$K^2 = \frac{U_E}{U_S} \tag{2.54}$$

where U_E and U_S is the stored electrical and elastic energy, respectively [22].

Piezomaterials are anisotropic. This means that the mechanical or electrical response differ with the axis of applied mechanical stress/strain or applied electric field. Thus, the directionality has to be accounted for when piezo activity is involved [49]. It follows that characteristics of a piezoelectric material are described by proportionality coefficients between mechanical and electric values, indexed with directivity. The axes are numbered 1 to 3 as shown in Figure 2.7. A coefficient linking measured electrical value along axis number i with corresponding mechanical action along axis j are indexed as X_{ij}.

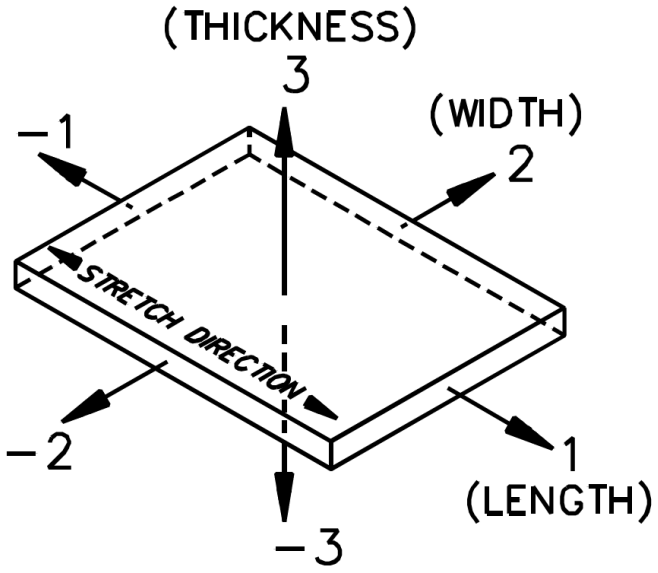

Figure 2.7: Axis numbering of a piezo element [49].

The most common piezo coefficients are d_{ij} and g_{ij}. The d_{ij} is a ratio of the electrical charge density on the surface of the piezo material, $Q[Coulumb/m^2]$, per mechanical stress on the same or another surface of the piezo material $F[Newton/m^2]$ [52],

$$d_{ij} = \frac{electric\ charge\ density}{applied\ stress} = \frac{\frac{Q_i}{A_i}}{\frac{F_j}{A_j}}, \tag{2.55}$$

where A_x is the area according to axis x.

The g_{ij} is the ratio of open circuit output voltage, V_0, per applied stress times the thickness of the material along the corresponding axis,

$$g_{ij} = \frac{V_{0,i}}{F_j z}, \tag{2.56}$$

where z is the thickness of the material in the appropriate direction [49].

We can use the same quartz example as in section 2.5.1 to describe another concept; *quality factor*. This time, neglecting the coupling factor, we look at the current as an applied oscillating force, and the mechanically oscillating quartz as a mass. Thus the piezoelectric effect can be viewed as a one dimensional mass-spring system. Although this is a crude simplification, the interpretation of the quality factor drawn from such a model can be transfered directly to the quality factor describing a piezoelectric ultrasonic transducer. The differential equation for an applied force of $Fe^{j\omega t}$ can be written as

$$\frac{d^2x}{dt^2} + \frac{R_m}{m}\frac{dx}{dt} + \omega_0^2 x = Fe^{j\omega t}, \tag{2.57}$$

where m is the mass, R_m is the mechanical resistance, x is the position and ω_0 is the resonance frequency of the mass-spring system [22]. Solving the differential equation with respect to x yields

$$x = \frac{1}{j\omega}\frac{Fe^{j\omega t}}{R_m + j\left(\omega m - \frac{k}{\omega}\right)} \tag{2.58}$$

where k is the rate of spring constant.

The velocity, $v = dx/dt$, is

$$v = \frac{Fe^{j\omega t}}{R_m + j\left(\omega m - \frac{k}{\omega}\right)} \tag{2.59}$$

Here we can see that the velocity lags the applied forced with a wave angle, θ, given by

$$\tan\theta = \frac{\omega m - \frac{k}{\omega}}{R_m} \tag{2.60}$$

Because of the phase lag, the power transfered to the oscillating mass-spring system is dependent on the frequency of the applied force compared to the resonance frequency of the system itself. The maximum power transfer occurs when these frequencies are equal. The bandwidth of a system is the width of the range of frequencies that occur. Often the full width half maximum (FWHM) measure of the power as a function of frequency is used to calculate the bandwidth. Finally, the quality factor Q, is defined as

$$Q = \frac{\omega_0}{bandwidth} \tag{2.61}$$

Thus a sharp and narrow power to frequency response around the resonance frequency gives a high quality factor.

The concept of directionality occur in many fields where energy is transmitted, such as electromagnetic antenna theory and, of course, ultrasound transducer theory. In the latter field it describes how the pressure of a sound wave transmitted from a transducer at frequency f, varies with angle. An example is shown in Figure 2.8, where most of the pressure is transmitted perpendicularly from the surface. This main lobe is calculated by identifying the direction of maximum sound pressure, and finding the angle of which this pressure is halved. The side lobes are calculated in a similar fashion. Although not shown in the

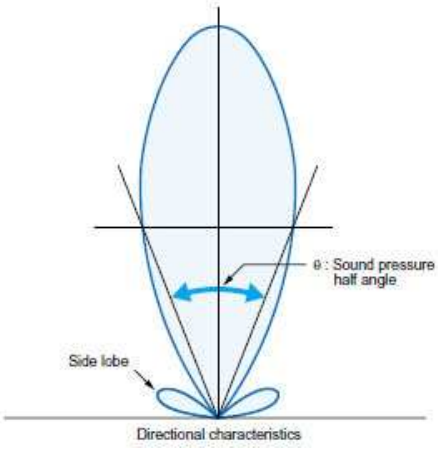

Figure 2.8: Example of directivity visualization

figure, there are in practice always some sound pressure emitted in the negative direction (positive being the intended direction). These sound waves may interfere with the positive traveling waves as they are subject to interfaces, which in most cases are undesirable.

2.5.3 Backing and matching layers

So far in this text we have not considered the media in which the piezoelectric materials are placed. As mentioned in section 2.5.2, some waves are launched from the rear face of the transducer. To avoid interference from these waves, a backing layer could be implemented. This layer should have an acoustic impedance as close as possible to that of the transducer, and a high attenuation coefficient. This means that the waves are accepted into the medium (reflection

coefficient ≈ 0) and attenuated. The thickness has to be designed so that most of, or all, energy has been absorbed before the reflection from the back end of the layer can reach the transducer. It is however possible to have a metallic backing. This will cause the waves traveling in the negative direction to reflect forward, and contributing to the amplitude of reflections from the target. It may however lead to more complex interpretations of the received signal.

To ensure that as much energy as possible reaches the intended target, e.g. in medical ultrasound imaging, the transducer front end can benefit from a matching layer. Without going into detail, a matching layers main purpose is to reduce the reflectance from the interface between transducer and target. Several different geometric approaches can be used, e.g. quarter wave matching layer [22].

2.5.4 Ferroelectricity in Polyvinylidene Fluoride film

A PVDF (Polyvinylidene fluoride) film is basically a normal polymer film which can be made ferroelectric after undergoing mechanical stretching and subjecting it to a strong electric field. This was discovered by Kawai in 1969 [52]. A ferroelectric material has both pyroelectric and piezoelectric effect, pyroelectric being a change in polarization due to a change in temperature. This means that when a ferroelectric crystal experience external effect such as physical stress, temperature change or a strong electric field, its polarization will change [52]. The reason for stretching the film is to change the molecular structure from a random-oriented crystalline structure to a semi-crystalline beta structure which has high piezoelectric properties [54]. In addition to the structural change, a strong electric field is applied in order to rotate the molecular dipoles in the same direction, and in effect polarizing them.

Because the PVDF films are very thin, the electrodes are placed on the "thickness" side shown in Figure 2.7. This means that the d and g coefficients are all indexed as d_{3j} and g_{3j}. When the film is used to measure force applied to its surface, d_{33} or g_{33} is applied. Changes in elastic properties due to stiff electrodes influence the characteristics of the film.

Some main advantages with PVDF transducers is the flexibility and size making them a good candidate to integrate into systems where space is limited.

2.5.5 Shape of the transducer and its influence on beam geometry

The physical shape of a transducer governs, to some extent, the shape of the propagating ultrasound field [38]. The area close to the transducer front end is called the *Fresnel zone*, or simply the *near field*. In this area, the field is propagating straight forward with little to non divergence. When the pressure

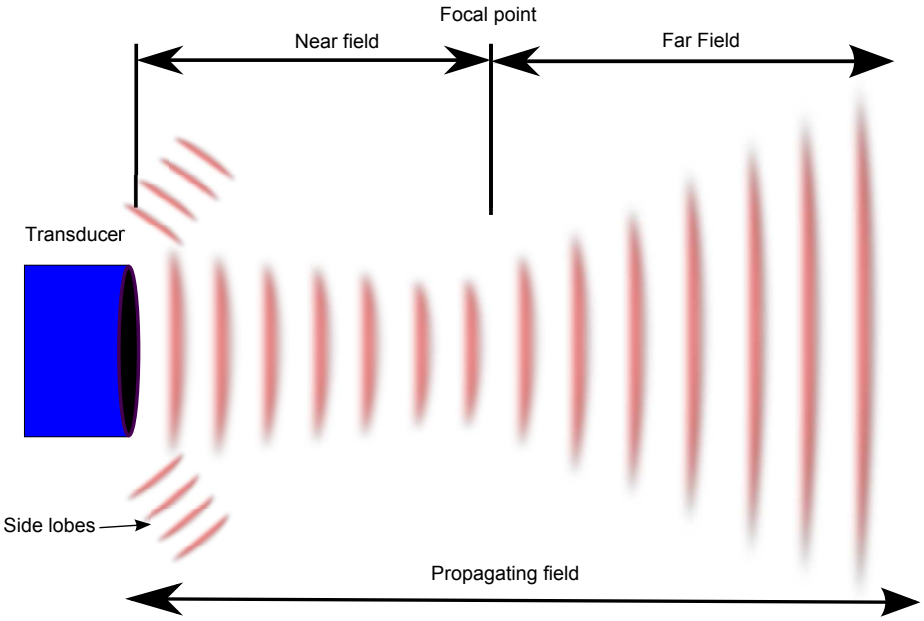

Figure 2.9: Field geometry. Length of near field depends on the geometry of the transducer front end, and wavelength of propagating wave

wave starts to diverge, it is said to have entered the *Fraunhofer zone*, or *far field*. Further manipulation of the pressure field is possible by applying a concave shape to the transducer front end. The length of the near field, L, is dependent upon both transducer geometry, frequency and the media in which the pressure wave propagates. For a circular transducer this can be expressed as

$$L = \frac{D^2}{4\lambda}, \tag{2.62}$$

where D = transducer diameter, and λ = wavelength in propagation media. Figure 2.9 shows a sketch of near-field and far-field behavior. In the case of rectangular transducers, the side length can be substituted into equation 2.62, but is not valid close to, or at the corners of the transducer.

The acoustic pressure from a rectangular transducer, of a specific position in space, $M(x, y, z)$, can be found by considering the contribution, dP, from every small element, ds, of the transducer front-ends surface, to the total pressure [27], [31]. The total pressure is then given by

$$P = \frac{j\rho c\mu_0}{\lambda} \frac{\exp(\omega t - kr)}{r} ds, \tag{2.63}$$

where ρ = density of the propagation medium, c = wave velocity, μ_0 = particle

velocity, ω = ultrasonic frequency, k = wave number and r = distance from the transducer.

For a rectangular transducer, the distance r from a small surface area $M_1(x_1, y_1, 0)$ to the point $M(x, y, z)$ is given by

$$r^2 = z^2 + (y - y_1)^2 + (x - x_1)^2 \tag{2.64}$$

Defining $y_0 = y - y_1$ and $x_0 = x - x_1$, we can rewrite r as

$$r^2 = z^2 \left[1 + \frac{(x_0^2 + y_0^2)}{z^2}\right] \tag{2.65}$$

Limiting the problem to points at a distance from the transducer, and near the z-axis, as shown in Figure 2.10, r can be approximated to be

$$r \approx z \left[1 + \frac{(x_0^2 + y_0^2)}{2z^2}\right] \approx R \tag{2.66}$$

where R is the distance from the center of the transducer. With this assumption it is possible to integrate over the transducer front ends surface to calculate the total pressure, P_M at point M.

$$P_M = \frac{j\rho c\mu_0}{\lambda R} \exp j(\omega t - kz)x \int_s \exp\left[-j\omega \frac{x_0^2 + y_0^2}{2z}\right] dx_0 dy_0 \tag{2.67}$$

In the article by J. Marini and J. Rivenez [27], it is shown how equation (2.67) can be rewritten to a form which shows both an amplitude and a phase term.

$$P_M = j\rho c\mu_0 \frac{\cos\gamma_0}{2} \sqrt{A_x^2 + B_x^2} \sqrt{A_y^2 + B_y^2} \exp j(\omega t - kz - \beta_1 - \beta_2), \tag{2.68}$$

where $\cos\gamma_0 = z/R$, $\beta_1 = \arctan(Bx/Ax)$, $\beta_2 = \arctan(By/Ay)$ and A_i and B_i are a sum of Fresnel integrals given as

$$\begin{aligned} A_i &= S\left[\alpha\left(i + \frac{a}{2}\right)\right] - S\left[\alpha\left(i - \frac{a}{2}\right)\right] \\ B_i &= C\left[\alpha\left(i + \frac{a}{2}\right)\right] - C\left[\alpha\left(i - \frac{a}{2}\right)\right] \end{aligned} \tag{2.69}$$

where $\alpha^2 = 2/\lambda z$. From equation (2.68), where the acoustic pressure at a point M can be calculated, the acoustic intensity at point M can be expressed as

$$I_M = |P_M|^2 / 2\rho c \tag{2.70}$$

It is also worth to notice that a square transducer with a given side-length of $A = x$ will have a smaller angle of divergence compared to a circular transducer with the same diameter, $D = x$. The equation for angle of divergence is given by

$$\sin(\eta) = k\frac{\lambda}{x}, \tag{2.71}$$

where x is side-length or diameter, k is a scaling factor and λ is wavelength. The scaling factor k is dependent on transducer shape and chosen power drop which is considered to still be in the main beam. Normally this power drop is at $-3dB$, or 50% of the maximum power. Appendix A lists these values of k.

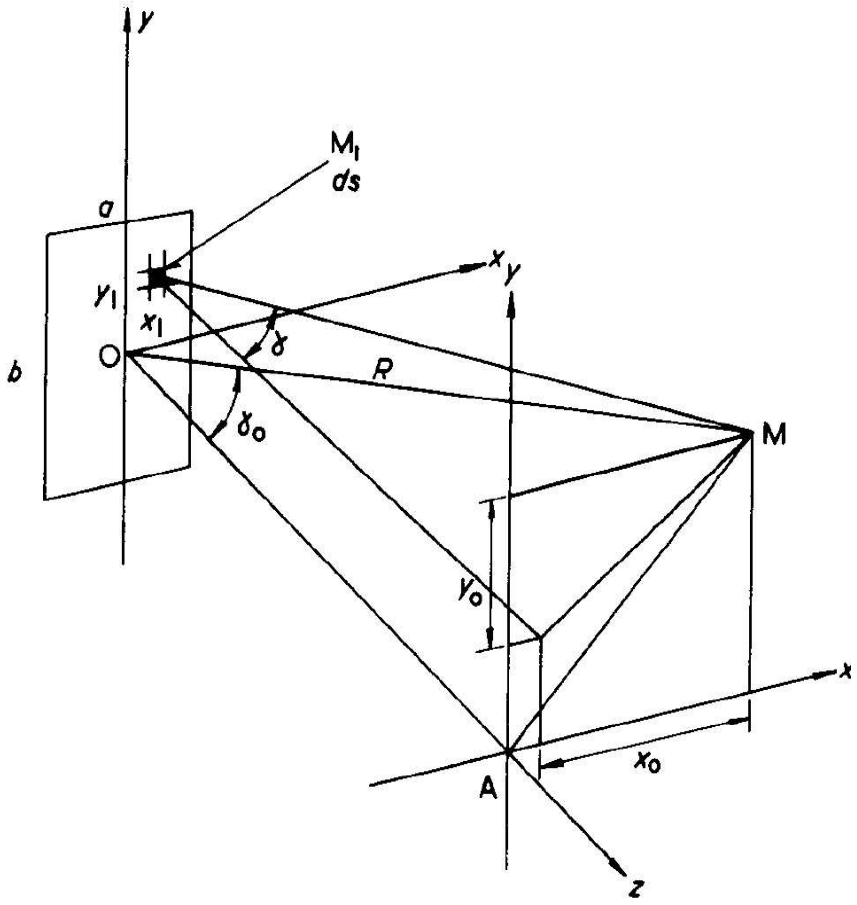

Figure 2.10: Geometry for calculation of the field from an rectangular transducer[27]

Chapter 3

Microwave heating system

The focus of this thesis is on the implementation of ultrasound in the described VUR diagnostic method. Ultimately, ultrasound measurements are a way to improve the quality assurance of microwave heating, and a closer look on the microwave antenna design, and impacts of implementing an ultrasonic transducer have on it, is therefore important. Antenna theory has a lot in common with ultrasound transducer theory regarding backing and matching, near field and far-field, directivity, etc. There are however differences which draws the two fields apart, the most fundamental being the type of waves transmitted. Although there might be some similarities to chapter 2, a short introduction to some aspects of antenna theory is included in 3.1.

The *specific absorption rate* (SAR) is the rate of which the body absorb energy when subject to an electromagnetic field, and is of utmost importance in microwave hyperthermia treatment. SAR can mathematically be expressed as

$$SAR = \frac{\sigma |E|^2}{\rho}, \tag{3.1}$$

where σ is the conductivity of the tissue, ρ is the mass density of the tissue and E is the rms electric field strength [32].

3.1 Antenna characteristics

The description of an antenna involves characterization of e.g. directivity, beamwidth, efficiency and gain. Such quantities are important for both design purposes and calculations regarding microwave heating.

An antenna radiation pattern is used to characterize the electromagnetic field generated by the antenna. It is found by calculating the magnitude of the

electromagnetic far-field strength at a fixed distance from the antenna versus position around the antenna [7].

Directivity is a way to describe an antennas ability to focus energy in a specific direction compared to other directions, and is defined as the dimensionless ratio of maximum radiation intensity to the average radiation intensity over all space [42],

$$D = \frac{U_{max}}{U_{avg}}. \tag{3.2}$$

For an arbitrary aperture antenna of which the current microwave antenna is an example, the maximum directivity possible to obtain is given by

$$D_{max} = \frac{4\pi A}{\lambda^2}, \tag{3.3}$$

where A is the aperture area, and lambda is the wavelength of the emitted microwaves.

The antennas efficiency is a ratio of the power supplied to an antenna, P_{in} to the power radiated by it, P_{rad},

$$\eta = \frac{P_{rad}}{P_{in}}. \tag{3.4}$$

Since most antennas are reciprocal, equation 3.4 is also applicable to received power.

Introducing an ultrasound transducer on the antenna surface will affect its efficiency as it blocks the aperture. The *aperture efficiency* is defined as the ratio of directivity to the maximum directivity found in equation 3.3,

$$\eta_{ap} = \frac{\lambda^2 D}{4\pi A}. \tag{3.5}$$

The antenna efficiency is always less than or equal to unity.

3.2 Radiometry

Radiometry is the scientific field of measuring and description of natural electromagnetic radiation, which mainly is of a thermal nature. Such radiation is emitted naturally by all atoms and molecules. A device to measure this radiation is called a radiometer. There are a vast number of scientific disciplines where radiometry is applied including oceanography, environmental research and medicine [26] [58].

The radiometer measures the noise power of the blackbody spectral radiation in its frequency band from a noise source at temperature T, which is mathematically described in the radiometer equation

$$P = kTB, \tag{3.6}$$

where k is the Boltzmann constant and B is the bandwidth of considered frequencies [9]. By introducing time and spacial dependency, the antenna power at time t can be written as

$$P_A(t) = kB \int_V W(x, y, z)T(t, x, y, z)dV, \tag{3.7}$$

where $W(x, y, z)$ is a weighted function dependent on the SAR pattern [9].

3.3 The VUR diagostic microwave antenna

The antenna design for the diagnostic method has been subject to research for a prolonged time period resulting in many different design approaches, some of which has been characterized in e.g. [12] [23]. The current microwave antenna consists of two antennas integrated on the same PCB. A dual concentric conductor (DCC) microstrip antennas at 915 MHz is used for heating, while a planar elliptical antenna, located at the center of the DCC antenna and connected to a 500 MHz bandwidth microwave radiometer with center frequency at 3.5 GHz is used for temperature measurements of the bladder [9]. The antenna is shown in Figure 3.1. The elliptical shape is the radiometric antenna, while the outer microstrips is the DCC antenna.

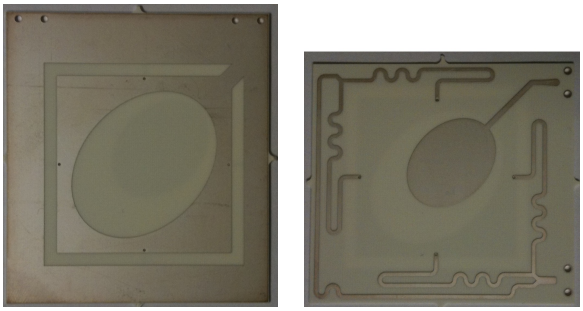

(a) (b)

Figure 3.1: Microwave antenna used for both receiving and transmitting. (a): Front. (b): Backside.

The DCC-antenna is constructed to have a 90 degree phase shift between each side, efficiently canceling radiation at the discontinuities of the corners. The

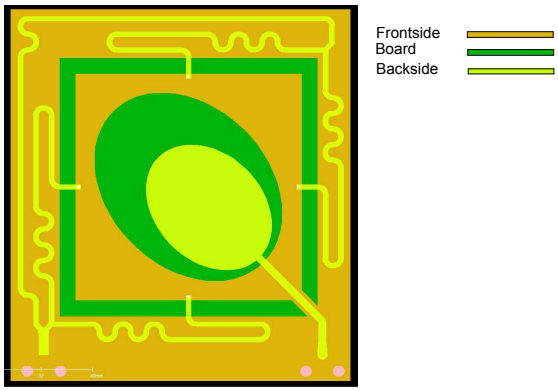

Figure 3.2: PCB layout of the microwave antenna.

feed line to both antennas are placed at a corner to minimize their effect on the emitted microwaves. Figure 3.2 shows the circuit board lay-out with both back- and front-side on the same side for visualization. The antenna apertures are the areas where the board (green) is visible. The PCB sides are 5.7 cm long.

Preliminary numerical simulations of the microwave antennas performance when a PVDF film is placed on its surface, has been conducted at the University of Tromsø [10]. The numerical model contained the microwave antenna (see Figure 3.2), a water layer representing the bolus, and human tissue layers sequentially placed as Table 3.1 indicates. The simulation was done in CST Microwace Studio[1] by transmitting microwaves with the DCC antenna and obtaining the resulting SAR pattern, both for heating and for radiometry. The simulation was first performed without introducing a transducer, and then repeated two times, first with a 4 mm and then with a 8 mm square PVDF transducer, both with electrical leads attached. Both transducers were placed at the center of the elliptical antenna and their leads introduced at the bottom right corner of the microwave antenna PCB as it is shown in Figure 3.2. The results from the simulation are summarized in Table 3.1.

	Initial	4 mm	8 mm	Initial	4 mm	8 mm
Bolus	42.9	45.4	45.5	65.1	77.3	78.1
Skin	46.2	45.9	45.0	61.3	60.2	60.4
Fat	13.8	13.7	13.0	17.9	18.6	18.4
Muscle	5.9	6.0	6.2	5.5	5.6	5.6
Bladder	32.5	32.8	34.1	15.0	15.4	15.4
Muscle	1.6	1.6	1.7	0.2	0.2	0.2

Table 3.1: Specific absorption rate with ultrasound sensor, DCC and elliptical antenna in left and right block, respectively [10].

[1]Software for electromagnetic simulations www.cst.com

Table 3.1 show the percentages of power deposited inside each layer incorporated in the simulations. The results for the bolus layer is presented as a percentage of total power, while the remaining rows are percentages of the remaining power. The DCC antennas performance (see the three left columns in Table 3.1), show an increase in deposited power inside the bladder for both transducer sizes. This entails that the DCC heating antenna performance is not affected in a negative manner by placing transducers at the center. However, turning our attention to the elliptical antenna (three right columns in Table 3.1) reveal an above 10% increase in the power deposited in the bolus when transducers are introduced. This means that the radoimeter recieves a weaker signal. As the signal strength is already very low, this is though to be an unacceptable increase of deposited power in the bolus, which leads to a reevaluation of the transducer placement attempted in this simulation.

Chapter 4

Methods

4.1 Signal processing and detection

4.1.1 Preprocessing

An acquired measurement can be viewed as consisting of two main components, namely a signal of interest and noise [24]. The noise can originate from anywhere in a signal's path between transmitting and receiving it. This includes electrical components, cross-talk between wires, irregularities in transmission medium, other signal sources, etc. In short, noise is found in almost all real-life acquired signals. A variety of methods to reduce or ideally remove noise is therefor widely utilized in signal processing.

As we will see later in this thesis, all obtained measurements have noise of both high and low frequency. It is possible to remove these noise components with minimal effect on the signal of interest, as long as their frequencies are outside the signals frequency band. This can be done by implementing a *bandpass filter*. Bandpass filtration lets a selected range of frequencies remain unchanged, while dampening the contribution of all other frequency components in the system. An ideal bandpass filter has a magnitude of 1 in the pass-band, and 0 for all other frequencies. The problem with this filter, is that its Fourier transform pair is a sinc-function, which results in ringing effects in the time domain. To avoid this effect we need a gradual transition in magnitude, instead of the ideal filter's abrupt change. In this thesis a 5th order *Butterworth bandpass filter* has been applied on raw data, which is a combination of a high-pass and low-pass Butterworth filter. It is therefor sufficient to look at the low-pass filter to explain the basic filter properties, which magnitude response can be written as

$$|H(w)|^2 = \frac{1}{1 + (\omega/\omega_0)^{2n}}, \tag{4.1}$$

where ω is the angular frequency, ω_0 is the angular cutoff frequency and n is the order of the filter. The cutoff frequency is defined as the frequency where the amplitude response of the filter is -3 dB from its maximum. The order n will in practice describe how fast the change from passband to stop band is, with regard to frequency. The higher the order, the quicker the change. As for the ideal filter, a high ordered filter will result in ringing effects in the time domain. The mathematical derivation of filter order can be found in [24], amongst others. Lets look at the artificial discrete signal, $s[k]$, which is a sinus wave with amplitude A and frequency f, sampled with a frequency of f_s.

$$s[k] = A \sin\left(2\pi f \cdot kT_s\right), \tag{4.2}$$

where $k = 0, 1, 2, ..., N$ is the sample number and $T_s = 1/f_s$ is the sampling rate. Random noise, drawn from a Gaussian distribution with variance σ and mean m, is added to the signal before receiving it. The received signal is thus

$$x[k] = s[k] + n[k]. \tag{4.3}$$

The goal now is to apply a Butterworth passband filter to reduce the noise in $x[k]$. An example of the filtration is shown in Figure 4.1. The transmitted signal has parameter values of $A = 1$ and $f = 10$ kHz. The added noise has variance $\sigma = 4$ and mean $m = 0$. The signal is sampled with $f_s = 200$ kHz. Filtration is performed with a 5th order Butterworth filter in Matlab[1] with the use of the functions *butter* and *filtfilt*. The filtfilt function applies both forward and backward filtration, which ensure no phase shift, and in practice doubles the filter order. The cut-off frequencies are $f_L = 9.5$ kHz and $f_H = 10.5$ kHz. The magnitude of the Fourier transform is shown in Figure 4.2.

The example shows us that although the received signal is completely drowned in noise, it can still be recovered with passband filtration.

Another preprocessing step applied in this thesis is time gating, which is to ignore samples prior to, or past a predetermined time. This has been applied on filtered data to remove both the first and last samples in measurements. The last samples are removed because they contain ringing effects caused by the Butterworth filter. The first samples are removed due to an effect introduced when using ultrasonic transducers in single mode. When a high voltage electrical pulse is sent to a transducer, an abrupt excitement of the piezo electric element occur. This initial fluctuation in the piezoelectric element will be converted back into an electrical signal, leading to a saturation in the measurement. This saturation is often referred to as the *main bang*[44]. Time-gating is therefore often included in preprocessing of raw data from transducers in single mode. All ultrasound measurements associated with the discussed VUR diagnostic method will be obtained through a water bolus. Since the water bolus has a minimum

[1] Techincal computational language and interactive environment delivered by Mathworks www.mathworks.com

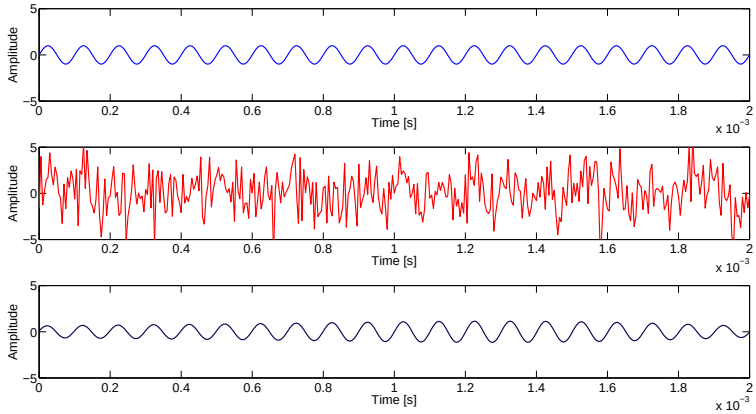

Figure 4.1: Top: Sent signal, $s[k]$. Middle: Received signal, $x[k]$. Bottom: Filtrated signal, $y[k]$.

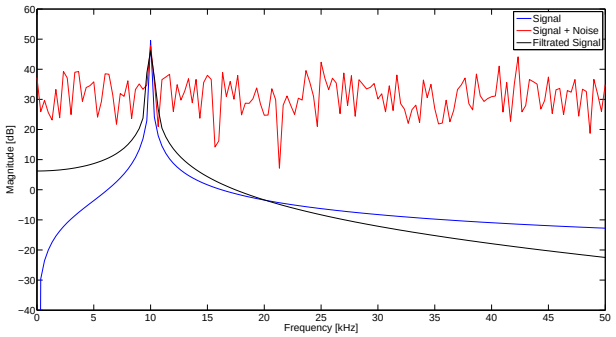

Figure 4.2: Magnitude of the Fourier transform for sent, received and filtrated signal.

thickness in the range of 2 mm, time-gating can be used without loss of any relevant reflections, for a time-period of $t_{TG} = 0.002[m]/c_w[m/s]$, where c_w is the sound speed in water.

4.1.2 Time of flight methods

Medical ultrasound and non-destructive testing (NDT) are often based on distance measurements. What is actually measured is the time difference between transmitting a pulse and receiving its echo, denoted as the pulse *time of flight* (TOF). Several different TOF estimation methods have been developed throughout the years [37],[3],[45], and choosing a suitable method is governed by e.g. system accuracy demands, environment surrounding the transducer, computational time (real time-measurement) and computational power limitations.

Amplitude thresholding

One of the most basic TOF estimation methods is probably time-domain amplitude thresholding. A measured amplitude larger than a predetermined threshold is defined as a pulse. This leads to the robustness of the test being highly dependent on the actual threshold. In medical diagnostics, differences in e.g. the placement of the transducer, or the curvature of individual patient's skin surface may result in relatively large amplitude differences in the pulse echo. Essentially this means that either the threshold should be recalculated in each diagnostics situation, or the system must be applied to each patient in such a way that the same amplitude is achieved every time. To make the system more practical, there is need for a more robust detection method.

Matched filtering

A popular method in TOF estimation is using matched filter. In simple terms, a matched filter involves finding the position in a received signal that best matches the sent waveform. Ultimately the matched filter was not utilized in this thesis, although attempted. Therefore we will constrain the discussion to some key equations and elements of the matched filter. A more in-depth description of the method can be found in [51] and [45].

If $s(t)$ is an arbitrary sent waveform, the filter that best matches it has, by definition, an impulse response of the form

$$h(\tau) = ks(\Delta - \tau), \tag{4.4}$$

where k and Δ are arbitrary constants [51]. This impulse response is the time-inversed signal, delayed by Δ, and scaled by k. Matched filtering is achieved by

convolving $h(\tau)$ with the received signal. This can also be done by multiplication in the frequency domain with $H(e(j\omega))^*$, the complex conjugate of the Fourier transform of $h(\tau)$. One of the main properties, and indeed one of the big advantages regarding robustness achievable with the matched filter, is that it maximizes the signal to noise ratio (SNR), which is given by

$$\rho = \frac{2\left[\int_{-\infty}^{\infty} S(j2\pi f)H(j2\pi f)e^{j2\pi f\Delta}df\right]^2}{N_0\int_{-\infty}^{\infty}|H(j2\pi f)|^2df}, \tag{4.5}$$

where $N_0/2$ is the *single ended* physical power density of the noise (only poisitve frequencies) and $S(j2\pi f)$ is the signals frequency spectrum [51]. A more applicable way of describing the SNR is

$$SNR = 20\log_{10}\left(\frac{P_{signal}}{max[P_{noise}]}\right). \tag{4.6}$$

This definition gives the SNR as a [dB] value, and is applied in Chapter 5. The famous Karlin-Rubin theorem also shows us that the uniformly most powerful test of size[2] α is a one-sided hypothesis threshold test [45]. Choosing a low size α to be constant in an hypothesis test is in many cases preferable to a high detection probability, e.g. it is better not to find the water bolus thickness than to make a false detection leading to an increase in microwave power, which might be harmful to the patient. Such a detector is called a *constant false alarm rate* (CFAR) detector. It has to be noted that Gaussian noise is assumed. It does not however require the noise to be white, as the noise can be pre-whitened [45].

The lab computer's I/O card and the transducers used in this thesis, has an unknown impulse response. This leads to the transmitted waveform also being unknown. Since we need a known waveform in order to apply matched filtering, an attempt was made to use a clear obtained reflection.

Energy envelope method

This detection method involves three main steps, in addition to the passband-filtration and time-gating to remove noise. Step one is calculating the energy of the recorded signal

$$E_n = \|x_n\|^2, \tag{4.7}$$

where E_n is the energy at sample number n, and x_n is the corresponding sample value [24]. Step two is to apply the finite impulse response (FIR) filter called *the running average* filter on the calculated energy. A FIR filter is a system

[2] Also referred to as the *false alarm probability*

where each output sample is the sum of a finite number of input samples [24]. An example of a running average filter can mathematically be described as

$$y[n] = \frac{1}{k}\left(x[n] + x[n+1] + ... + x[n+(k-1)]\right), \tag{4.8}$$

where $y[n]$ is the running average filter output at the discrete sample number n, $k = 2, 3, 4, ...$ is the window size, and $\mathbf{x}$ is the input vector [24]. As equation (4.8) shows, each output sample is the average of k input samples. The example takes the mean of sample n and the $k-1$ next samples. The running average could also have been the k previous samples, or $p = k/2$ samples on each side of sample n. In our case it is important to detect the first reflection, and thus we prefer to use the forward looking running average to get a large response at the beginning of a received pulse. The size of k was determined by the length of a reflection. This means that there should be a clear peak in the output vector $\mathbf{y}$ at the start of a reflection. This quantity can be viewed as the signal power, as it is the average energy in the reflection length.

The last step in the detection algorithm is to identify which peaks in the running average output vector are actual reflections. Selecting e.g. the maximum amplitude will always return a sample number, regardless if this corresponds to a peak or not.

Thresholding before selecting the maximum amplitude is an obvious approach to avoid this problem. This could however result in many *false alarms*, or false detections, if an unknown noise source or undesirable reflection manages to raise the noise/signal power in measurements. An concrete example of where such unwanted reflections may arise is found when air gaps between the transducer and the water bolus appear. This will lead to a large reflection appearing very early in the time signal due to the large acoustic impedance difference between air and water/ultrasound gel. Although these type of reflections are time-gated out, two unwanted effects from a large early reflection influence the remainder of the measured signal. First of all, almost all pulse energy is reflected back at this first *unwanted* reflection, leaving only a small portion left actually traveling through the water bolus. This will result in a very small reflection from the bolus-patient interface at best. The second unwanted effect is ringing from the first reflection, coupled with multiple reflections between the transducer surface and the air gap, which will worsen the detection probability even further. For transducers implemented on the VUR diagnostic antenna, these types of effects are further increased by the poor acoustical backing offered by the PCB card, as some of the transmitted pressure wave will travel in the negative direction and reflect back to the transducer at the PCB/microwave backing material interface.

In an attempt to avoid these false alarms, or reduce the probability of them occurring, a Matlab function called *peakdet* was implemented. This function is not included in Matlabs signal processing toolbox, but can be found on-line as an open source function and has been applied in the literature in e.g. genetics [13]. A sample $x[n]$ is considered a peak if it is presided by a sample with

amplitude lower than a set parameter, $x[n] - x[n-1] > \Delta A$. In addition, a valley, or minima, has to be found in the same manner before looking for additional peaks. If a second peak is found prior to a valley, the peak with the largest amplitude of the two is selected. This is almost like looking at the gradient of the power. After all peaks have been identified, the maximum is selected as the actual reflection.

4.2 Acoustic properties of soft tissue and phantom materials

Medical ultrasound imaging and ranging techniques are dependent on accurate knowledge of the acoustic properties of tissue. Properties such as attenuation, density, acoustic impedance and velocity are dependent on each other, and all affect how ultrasound propagate through a medium. Consider a single transducer used for both transmitting and receiving, placed on a patients skin surface. A percentage of the sent pulse will reflect of the interface between two tissue types with different acoustic properties. The amount reflected is described by the reflection coefficient, which can be calculated from (2.28). The reflection coefficient is determined by the acoustic impedance of the media, which in turn is governed by the density and sound speed, as shown in equation (2.21).

What we measure is a time signal with a received pulse at a time instance t_r. In ranging, where the distance is unknown, this information is useless without a known sound speed in the tissue. Attenuation in tissue, together with the reflection coefficient, is also important to estimate the amplitude of received signals. It has to be noted that scattering effects further demises the reflected signal amplitude.

The accuracy of a distance measurement is determined by the accuracy of the sound velocity in the tissue and the precision of the detection method used to determined t_r. From an ultrasound system design aspect, the acoustical properties of tissue, and ways to mimic them in a controlled lab environment, are thus key factors in order to obtain accurate thickness measurements.

4.2.1 Body tissue

In development, characterization and calibration of medical ultrasound systems, tissue mimicking materials with known properties are required. Since the 1960s, several different materials has been found, developed and/or tuned, to have the same properties as different parts of the human body, e.g. skeleton, organs, blood veins, skin etc [25], [17],[57]. Table (4.1) lists acoustic properties of some selected tissue types, and for reference, air and water.

Material	Velocity [m/s]	Density [kg/m^3]	Attenuation [dB/cm MHz]	Acoustic Impedance [MRayl]
Air	330	1.2	-	0.0004
Breast	1510	1020	0.75	1.54
Fat	1478	950	0.48	1.40
Muscle	1547	1050	1.09	1.62
Skin (Fetal)	1540	1.1-1.19	9.2 ± 2.2	1.71-1.83
Soft tissue (average)	1561	1043	0.54	1.63
Water	1480	1000	0.0022	1.48

Table 4.1: Table of acoustic properties for human tissue. Water and air are listed for reference. [36]

4.2.2 Phantom materials

The basis of a phantom is often a homogeneous material, which can be further modified with additional ingredients to alter temperature resistance and scattering properties, amongst other. Table (4.2) lists some of these bases and their general acoustic properties.

There are a variety of ready made tissue phantoms which can be bought. These phantoms are often tailored for a specific use, e.g. calibration of a commercially developed ultrasound imaging system. In addition they are often quite expensive, ranging in price from hundreds to thousands of dollars. The alternative is to make phantoms, which often allows for easy customization with regards to dimension, structural and acoustic properties, but great care has to be taken to ensure a result with correct acoustical properties. Some of the different methods to manufacture an ultrasonic phantom can be found in [36].

Material	Velocity [m/s]	Density [kg/m^3]	Attenuation [dB/cm MHz]	Acoustic Impedance [MRayl]
Agarose-based	1498 - 1600 +	1016 - 1100	0.04 - 1.40	1.52 - 1.76+
Agar 2%	1500 ± 0.03	1040 ± 110	0.4-0.5	1.57 ± 0.08
Gelatin-based	1520 -1650	1050	0.12- 1.5	1.60-1.73
Magnesium Silicate -based	1458 - 1520	-	0.85	-
Oil Gel-based	1480 - 1580	1040 -1060	0.4-1.8	1.54 - 1.67
Polyuerethane	1468	1130	0.13	1.66
Water-based	1518 - 1574	1000+	-	1.48 - 1.60

Table 4.2: General acoustical properties of some phantom bases, and the specific phantom utilized in this project.

4.2.3 Selected tissue phantom

The main focus in this thesis is the interface between the water bolus and the human body. Therefore we want a interface which closely matches that of skin and fat, which are the first layers an ultrasound beam will encounter. An article by K. Zell gives detailed properties and method for manufacturing four different tissue phantoms [29]. The agarose-based phantom described in the mentioned article was chosen for its close acoustical match to breast tissue, and its relative simple preparation method. Although a gelatin-based phantoms acoustical impedance is closer to fetal skin, a detailed description of how to obtain the different values of the relatively wide range in the reported acoustical impedance was not found. Additionally, acoustic properties of skin might vary throughout a patients life. Thus a *worst case scenario* of a skin surface with acoustic properties close to that of agarose-based phantom was a natural approach. The big difference in attenuation have been neglected as we are initially interested in the first reflection. One may argue that the structural differences between the homogeneous phantom and human tissue will further demise its relevance, but although internal structures will influence an *in-vivo* obtained data through scattering effects, the impact on the first reflection are assumed negligible. The chosen phantom was prepared according to the following method. A 2% agar-powder, 98% distilled water mixture is heated to 98° C, and kept at this temperature under constant stiring for about 10 minutes, until the mixtture becomes viscouse and clear. Then poured into a mould and refrigerated until the mixture becomes solid.

Steps were taken to ensure a close match between the acoustical properties of produced tissue phantom and the values reported in Table 4.2. The sound speed was measured to find out deviations between the self-made phantom and the reported sound speed in [29]. The agar-phantom was allowed to reach room temperature by leaving it out over night. Then the phantom was placed on a acrylic glass surface with ultrasound gel in between. A 12x30 mm^2 rectangular transducer of type FLDT1-052K [48] was placed on top of the phantom. The backing material used was the microwave antenna with its own backing used for heating in the VUR diagnostic set-up. A total of 30 measurements was acquired, each an average of 1000 sent and received pulses. The actual phantom thickness was found by using a electronic caliper ruler with a resolution of 0.01 mm. Because of the elastic nature of the phantom, no external pressure was applied to the transducer during measurement to allow for the same phantom thickness when using the caliper ruler. To further increase the accuracy of this measurement, only the backing material was removed, and the thickness on each side of the transducer was measured by using the extendable pin on the far end of the caliper ruler to penetrate through the agar-phantom. A third thickness measurement was also acquired in the same manner, after removing the transducer, directly below the transducers position. To calculate the sound speed, the simple relation

$$v = d/t, \tag{4.9}$$

where v is sound speed, d is distance, and t is time, was used. The pulse time of arrival is found by using the Energy envelope method described in 4.1.2.

The density of the phantom was found by measuring the weight and the amount of water the phantom slab displaces. The weight used has an resolution of 0.1 mg, and the water displacement was measured in a water filled thin test tube with a resolution of 0.1 ml. The density is then found with

$$\rho = [gram]/[ml] = [kg]/[m^3]. \tag{4.10}$$

4.3 Transducer design

When implementing an ultrasound transducer into the current VUR diagnostic system, care has to be taken to minimize destructive effects to the microwave field such as effect loss and field distortion. In this text, *transducer design* entails mainly the antenna dimensions and how these affects the ultrasound beam. Spatial dimensions of the ultrasonic transducer is limited by the microwave heating system.

The diversity of ceramic piezoelectric materials allow for a wide variety in elastic, piezoelectric and dielectric constant. In general this leads to these materials having the most favorable properties for ultrasonic transducers. Ceramics can also be made in a variety of shapes and thus be tailored for specific applications [19]. The drawback is that once finished the transducers are hard and brittle making them inflexible. In contrast, PVDF film transducers are flexible and thin. For placement in between the microwave antenna and the bolus, a transducer element thickness of any significance will influence both microwave hyperthermia and radiometric readings. A PVDF film is therefore viewed as the most plausible transducer type for integration into the VUR diagnostic system.

The shape of a transducer front end affects the propagating ultrasonic pressure field as discussed in chapter 2.5.5. Ready made rectangular transducers were attempted implemented in this thesis. They are delivered with electrodes attached, and can be modified into an arbitrary shape. To achieve a satisfactory accuracy, the modifications has been limited to straight cuts for practical reasons. Data sheet for the rectangular PVDF film used in this project can be found on the manufacturers web page [48].

Loosely said, the smaller the surface area of the transducer front end, the wider the main beam is in the far field. A desirable property of the final transducer design is to get a clear reflection in measurements even when the transducer plane deviates from being parallel with the patients skin surface. This can be ensured by increasing the main lobe width through reducing its size. The cost

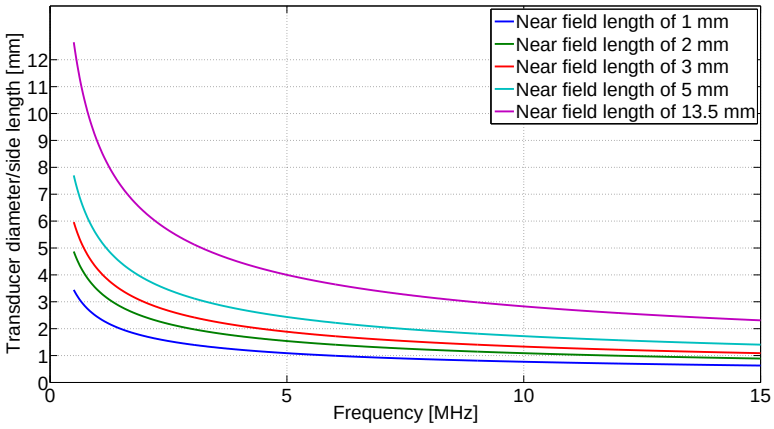

Figure 4.3: Lines indicate different near field length in water at 20°C as noted in the figure legend.

being a reduction in emitted, and thus received, energy. Equation (2.70) was implemented in Matlab to illustrate the effect of reduction in transducer front end surface area on the main lobe width of the pressure field.

Preliminary data has shown that the rectangular transducers used in this thesis has an approximate center frequency of 5 MHz, which in water at 20° Celsius corresponds to a wavelength of $\lambda_w = 1482[m/s]/5 \cdot 10^6[Hz] = 0.2964[mm]$. The length of the far-field can then be found with the aid of equation (2.62), which result is shown in Figure 4.3.

As Figure 4.3 shows, a near field length lower than 2 mm at 5 MHz requires the transducer diameter (circular) or side-length (rectangular) to be lower or equal to 1.5 mm. The 4 mm transducer has a near field length of 13.5 mm. The near field length is dependent on both frequency and transducer surface area. The ultrasound frequency is dependent on both the frequency content of the transmitted pulse and the transducers frequency response. In this thesis the applied frequencies were limited by the available ultrasonic I/O card which uses a standard square pulse with a tunable length.

The width of the transmission lines of the transducer restricted the minimum side length and shape of the cropped transducer. This led to the manufacturing and testing of circular transducers. A PVDF film will expand or contract when placed in an electric field, as described in section 2.5.1. Making circular transducer can thus be achieved by altering the size and shape of the electric field instead of the PVDF film size. A printable circuit board (PCB) was etched out with four different transducers, as shown in Figure 4.4.

The circular shaped pads are transformed into transducers by gluing a single

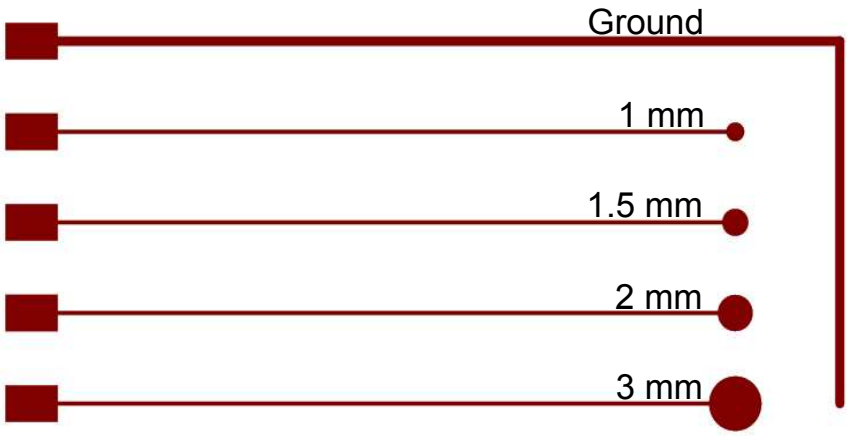

Figure 4.4: PCB layout. Ground is always connected, while aperture size is optional.

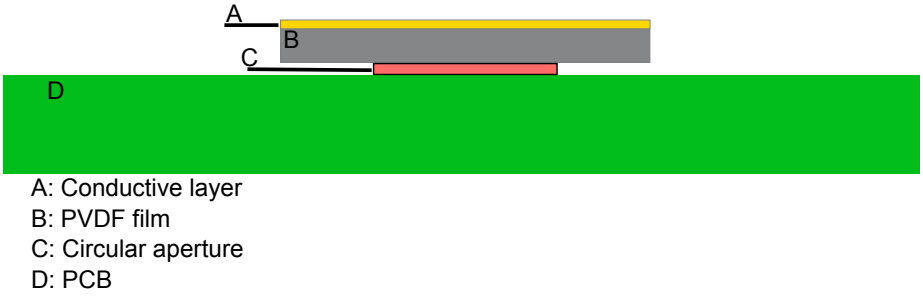

Figure 4.5: Layers of the manufactured transducer seen from the side

PVDF film [41], with a fixed conductive side pointing out and connecting the conductive surface to ground. In Figure 4.4, the layers of the manufactured transducers are shown from the side.

Some considerations had to be made before manufacturing could begin. First, the PVDF films films can not endure high temperatures. This means that all soldering had to be done prior to attaching the PVDF film. For the same reason, a conductive glue which hardens at 80 degrees $C°$ was used to connect the conductive upper surface to ground [20]. The PVDF film was glued over the circular apertures with an epoxy. The thickness of the epoxy was kept at an minimum to minimize the effect on the transducers conductance. As explained in section 2.5.4, stiff electrodes might change the characteristics of a PVDF film, and the conductive glue was kept at a distance from the active regions. The PCB card will also work as backing layer for the transducer. The resulting *four in*

one transducer is shown in Figure (4.6). Originally, the ground was intended to be connected to the PVDF film at the center of the PVDF rectangle. Attaching the PVDF film to the PCB with epoxy resulted in a thin unwanted epoxy layer covering this intended connection point on the ground line. Therefor, the connection between ground and PVDF film was made at the position shown in Figure 4.4. The frequency range of the transducers used in this project has a upper limit of about 15 MHz.

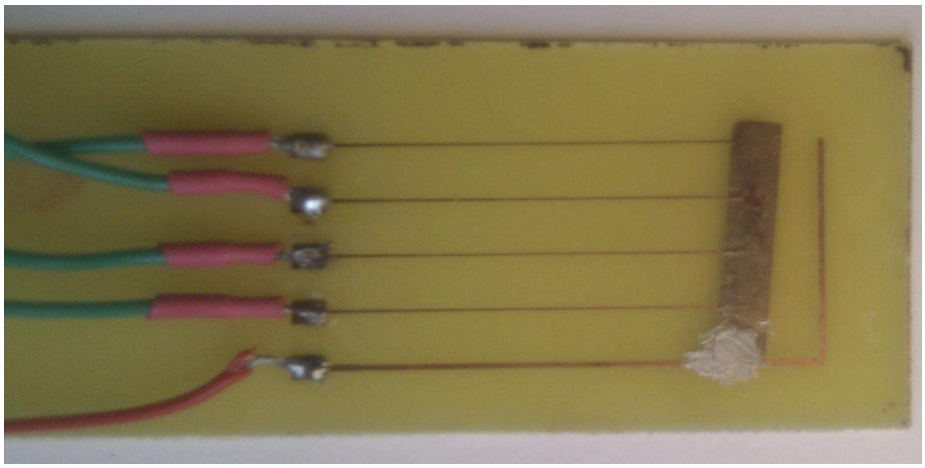

Figure 4.6: Circular transducer PCB. The golden strip to the right is the conductive top layer. On close inspection, the four transducer apertures are barely visible through it.

4.4 Transducer position

Water bolus thickness may vary across its surface due to the elastic plastic material it is comprised of, water flow and applied pressure when placing the bolus on a patient. Positioning the ultrasonic transducer to measure the water thickness directly below the microwave antenna is therefore vital to achieve accurate measurements of the water contribution to microwave absorption. Thin PVDF films, which can be directly mounted on the microwave antenna, should therefore be well suited for this application.

Despite the limited surface area available of the microwave antenna, there is a possibility for multiple transducers. With a single transducer, used for both receiving and transmitting, the pulse shape has to be short, so that the transmitted pulse does not interfere with the received. This reduces the possible waveforms greatly because of the relative short distance of which the wave can travel (ca. 6 - 20 mm). Using dedicated transducers, that either transmit or receive pulses, should allow for other, longer waveforms. An example of such

a pulse is the chirp signal. A chirp is a sinusoidal signal with an increasing or decreasing time-dependent frequency,

$$s(t) = A\cos\left(2\pi f(t)t\right). \tag{4.11}$$

The frequency change may be linear, $f(t) = f_0 + kt$, or exponential, $f(t) = f_0 k^t$, where k is the chirp rate. To avoid aliasing, the signal need to be stretched out in time for broad-banded signals. One of the advantages of chirp signals is that they have a quasi-rectangular frequency window, allowing full use of the transducer bandwidth. In addition to opening up the possibility for a larger pulse duration, it also reduces the minimum length detectable. When a single transducer is used it starts *listening* as it sends the pulse. This causes the received electrical signal to be saturated during the time laps when the transducer is transmitting. Although a very short pulse is transmitted, ringing effects from this initial displacement in the transducer will in most cases endure, leading to distortion of any received signal. Utilizing dedicated transducers should remove this effect.

Multiple receivers will increase the need for beam width even further as the beam from the transmitting transducer should be able to reach all the receiving transducer at an angle, as shown in Figure 4.7. However, having three or more receiving transducers may allow for calculation of the angle between the transducer plane and the patients skin. This angular information could be useful for an operator, as it provides information regarding the direction of microwave emission. Alternatively a minimum of three transducers in single mode can be used.

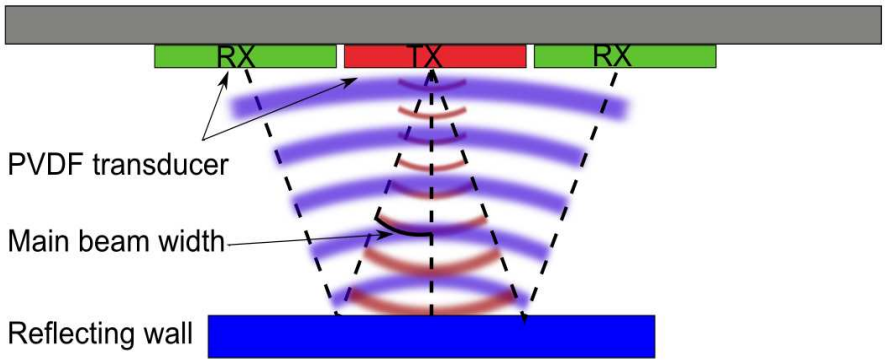

Figure 4.7: Beam width needed in the case of dedicated transducers.

4.5 Experiments

4.5.1 General aspects of the experiments

In all data acquisition, a US Ultratek PCIUT3100 pulse receiver has been used to both transmit and record the signals. The transmitted signal is a square pulse with a time extent of 50 ns. A sampling frequency of $f_s = 100$ MHz, voltage of $U = 200$ V and a number of sample $N = 4000$, was used throughout the experiments. All obtained signals is an average of a 1000 sampling vectors. Ultrasound gel was applied between all layers, e.g. transducer front end and bolus, to ensure good acoustic contact. To process the data, Matlab and its signal processing toolbox was used.

4.5.2 Antenna main lobe

This experiment is conducted to establish the main lobe width for different transducer sizes and shapes. Comparison between a 8x8 mm rectangular transducer, which operates in its near field, and smaller transducers in their far field is also of interest.

A relatively wide beam has to be achieved for the VUR diagnostic application, regardless of whether a single transducer or multiple transducers are to be used. For a single transducer, small angular differences between the transducer plane and the patients skin must still produce a clear reflection. If two dedicated transducers are to be used, even greater beam width must be achieved, both to reach the receiving transducers, and to achieve robustness similar to that of a single transducer.

Procedure

Figure 4.8 shows a schematic plot of the complete experiment setup. The top plate was locked in place using the vice, and adjusted to a horizontal position using the bull's eye spirit level. To avoid air between layers ultrasound gel was applied between the bolus and both the transducers and the reflecting layer. The water volume inside the water bolus and the thickness below the antenna were kept constant. When the screws are turned, the water pressure ensures a close contact between transducer and bolus for all angles. Four circular transducers and two rectangular transducers were tested. The circular transducers had diameters of 1, 1.5, 2 and 3 mm, respectively, while the rectangular had surface areas of 4x4 mm^2 and 8x8 mm^2. A single transducer were placed on top of the water bolus, parallel to the reflecting layer beneath it. The angle between these two layers were then gradually increased. To calculate the angle between the PVDF films surface and the layer beneath the water bolus, the length between the top and angled plate were measured using a caliper ruler, for each data

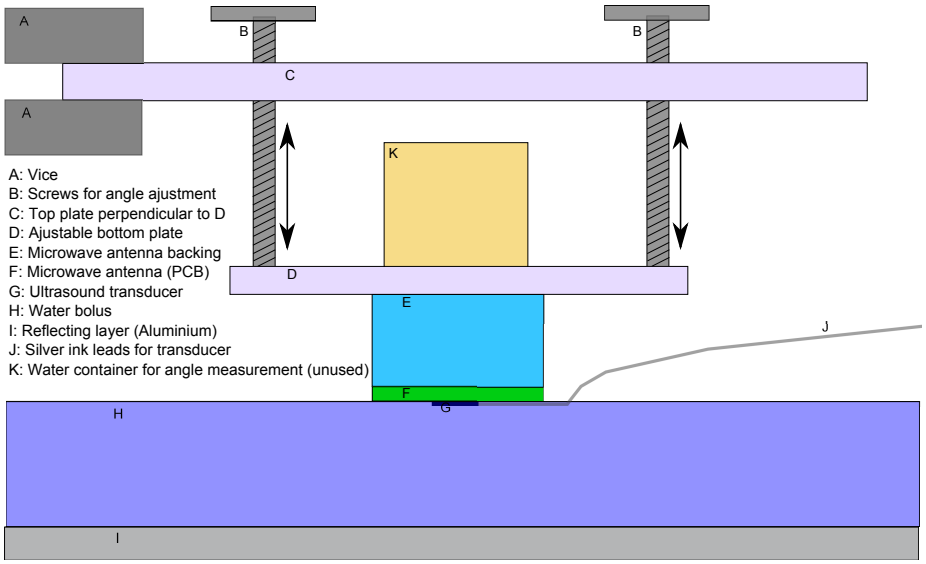

Figure 4.8: Experimental setup used in antenna main lobe measurements.

acquisition. The hight difference, h, and the length of the angled plate $l = 80mm$, was used to calculate the angle, ϕ, between the reflecting surface and the transducer as

$$\phi = \tan^{-1}(\frac{h}{l}). \tag{4.12}$$

For each of the PVDF film sizes, measurements were acquired at approximately the same angle. The experiment was conducted two times to increase the reliability of the results. As rectangular transducers have discontinuities at the corners, these transducers were repositioned in the transducer plane, as shown in Figure 4.9.

The data was filtered, and reflections were detected using the energy envelope method, described in section 4.1.2. To calibrate the method for a idealized reflecting wall, the defined reflection length, used in the running average filtration step, was increased from 60 samples to 400 samples.

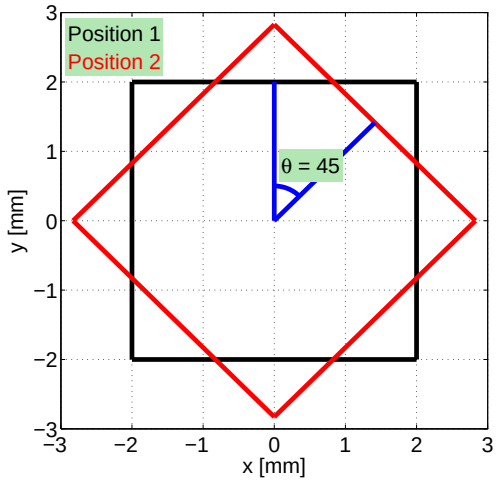

Figure 4.9: Perpendicular view of the transducer plane. The rectangular transducers were originally in position 1. For evaluation of effects at the corners, measurements were also acquired with transducers in position 2.

4.5.3 Transducer size and detection

This test was conducted to compare pulse detectability for different sized transducers at increasing distances from patient skin surface. Four circular transducers, with diameters of 1, 1.5, 2 and 3 mm respectively, were tested. Increased distance was achieved by increasing bolus thickness. Comparable measurements with the reflecting phantom tissue surface substituted with an ideal reflectable surface in the form of an Acrylic glass plate were also conducted. reflect

Procedure

A programmable linear actuator was used to reposition the transducers during the experiment, as shown in Figure 4.10. The water bolus and a reflecting layer (acrylic plate or phantom) were locked in place next to the transducer front end. At the beginning of each measurement, the water bolus thickness was set at 1 cm. This was achieved by measuring the thickness between the transducer front end and the reflecting layer on the opposite side of the water bolus. The linear actuator was used to tweak the bolus thickness until the one cm mark was reach. Measurements were acquired at distances from 10 mm to 4 mm, at an interval of 0.5 mm. The distance reduction was achieved by using the linear actuator to force the water bolus thinner. This resulted in increased water pressure inside the water bolus. This increased pressure exerted a force on the transducer mount extended below the linear actuator rail, resulting in the

transducer mount being bent to a small extent, instead of a full 0.5 mm reduction in water bolus thickness. To counteract this, water filled tubing was attached to one of the water bolus outlets, thus allowing water to flow out of the water bolus as its thickness was reduced. The tubing was coiled at approximately the same height as the water bolus allowing water to flow back when the pressure on the bolus was reduced. A time-lap between altering bolus thickness and measuring with a transducer was implemented to let the water pressure reach equilibrium. The experiment was repeated ten times for each of the ultrasound transducer sizes. Figure 4.11 shows the set-up during data gathering, and Figure 4.12 shows the water bolus with phantom material as reflecting layer. The water filled tubing is also visible. The water temperature was measured to calculate the sound speed, according to Lubber and Graffs' simplified equation [39]. Post-processing of the data included filtration and detection in accordance with the description in section 4.1.1 and 4.1.2, respectively.

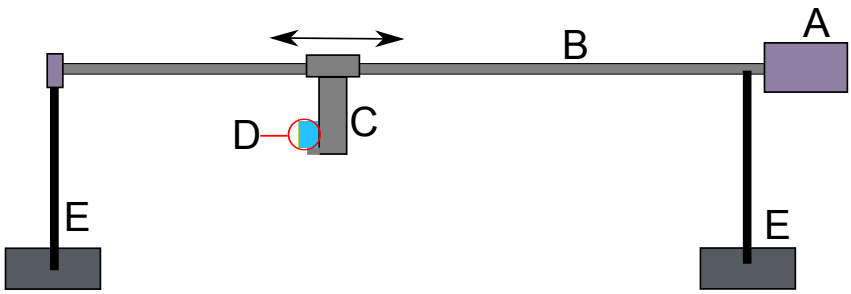

A: Linear actuator motor
B: Linear actuator rail
C: Transducer mount
D: Ultrasound transducers and backing
E: Stands with manual hight regulation

Figure 4.10: Schematic plot of the linear actuator.

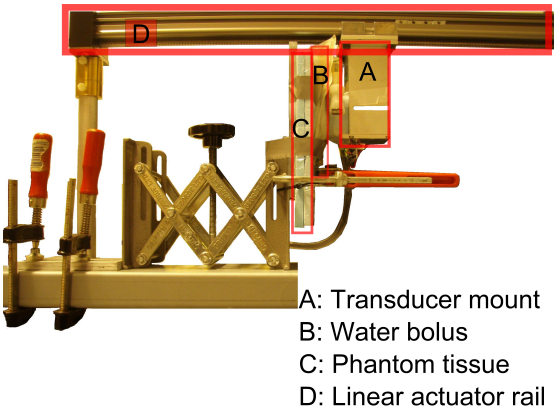

Figure 4.11: Complete set-up in use. The transducer and its backing is located between the transducer mount (A) and the water bolus (B), but is hidden by the water bolus inlet

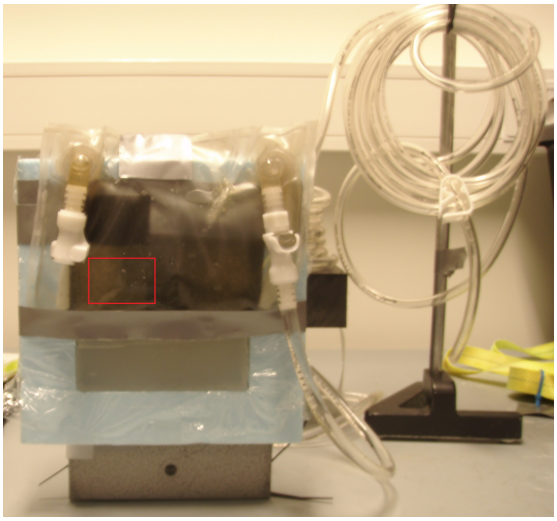

Figure 4.12: Bolus and phantom as used in detection experiment, seen from the front. Red rectangle indicates the area where the measurements were taken. The water filled tubing is visible to the right.

4.5.4 In vivo

Measurements were taken with both circular and square transducers, with human stomach as reflecting wall, to find the reflection size and its detectability.

Procedure

Ultrasound gel was applied to the subjects stomach before placing the water bolus. The transducers were held in close contact with the bolus during data acquisition, and adjusted by hand to be in a parallel plane with the skin surface. Measurements with a deliberate misplacement, resulting in the transducer plane and the skin surface being unparallel, were also attempted. No verification of the actual bolus thickness was obtained.

Chapter 5

Results

5.1 Tissue phantom properties

The following results were obtained to verify the acoustic properties of the Agar based phantom tissue used in this thesis.

As explained in section 4.2.3, we need to measure both the phantom tissue's thickness and the time lap between transmitting and receiving an acoustic pulse to determine the sound speed. Three measurements of the phantom thickness were acquired using an electronic caliper ruler, with a mean value of 18.46 mm. Since a transducer in single mode was used to measure the TOF, this distance had to be doubled before using it in the sound speed calculation, as the ultrasonic pulse distance of flight (DOF) is twice this length, $DOF = 36.92$ mm. The actual thickness measurements are shown in Table 5.1.

The uncertainty of the found thickness was chosen as two times the standard deviation of the measurements obtained by caliper ruler, and found to be 0.605 mm. This uncertainty gives rise to the uncertainty in the calculated sound speed, reported in Table 5.2.

The time of flight was acquired by taking the mean of 30 measurements obtained with a PVDF film transducer, and found to be $TOF = 24.75$ us.

Measurement number	1	2	3
Measured dist [mm]	18.34	18.63	18.41
DOF [mm]	36.68	37.26	36.82

Table 5.1: Measurements obtained with electronic caliper ruler.

Reported sound speed [m/s]	Found sound speed[m/s]
1500 ± 3	1491.7 ± 20.2

Table 5.2: Calculated sound speed in the Agar 2% phantom tissue material. Reported sound speed is found in [29].

Table 5.3 shows the measurements obtained to calculate the density, together with found density. Similar to the approach used in the sound speed calculation, the uncertainty of the density is based on the resolution in the measurement of displaced water.

Weight [gram]	Displaced water [mL]	Density [kg/m^3]	Reported density [kg/m^3]
5.1582	5.0	1040 ± 110	1032

Table 5.3: Values for density calculation.

By applying equation (2.21) to the found results, the acoustic characteristic impedance can be calculated,

$$Z_0 = \rho_0 c_0 = 1.539 MRayl.$$

This calculated acoustic impedance in the range of breast tissue (see Table 4.1).

5.2 Antenna main lobe

Before looking at the data from the experimental work regarding the transducers main lobe width, we will consider some numerical results which illustrate what we can expect. In Figure 5.1, the acoustic intensity in a cross-section, obtained from equation (2.70), located 2 cm from a 4x4 mm transducer is shown. At this distance, the propagating pressure wave is located in the far field. A notable drop in divergence is observed around the corners of the rectangular transducer, which is located at the center of the figure.

In Figure 5.2, the expected relation between main lobe angle and transducer front end size, based on equation (2.71), is shown. The scaling factor k is chosen for a -3 dB drop in the power ratio and is 0.51367 for circular transducers and 0.44224 for rectangular transducers (see appendix A). Dependency on wavelength means that a sound speed and frequency must be defined. The sound speed was set to corresponding to the theoretical velocity in 20°C distilled water, which is 1482.3 m/s. A center frequency of the circular transducers has been observed to lie in the range from 4.5-7.5 MHz, so the lines are computed for the center frequency in this range, which is 6.25 MHz. Observe that the expected transducer main lobe width for the selected transducer sizes are in the range from 0.8 to 7 degrees.

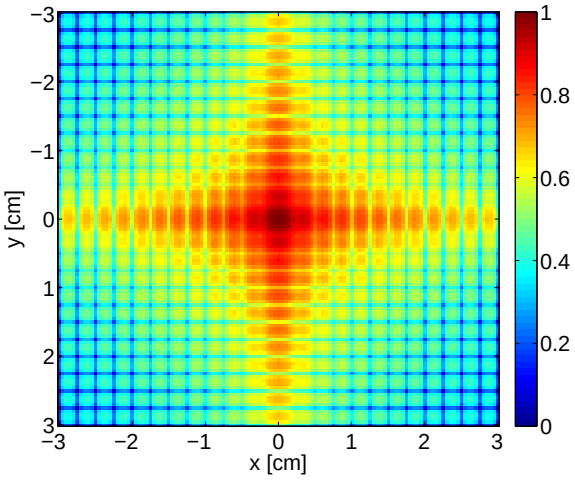

Figure 5.1: Theoretically obtained cross-section, or xy-plane, of the acoustic intensity at a distance of $z = 2$ cm from a 4x4 mm transducer front end.

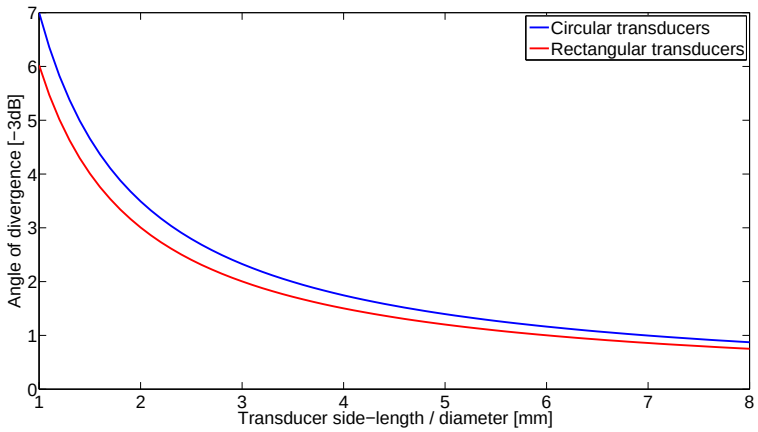

Figure 5.2: Angle of divergence, or beam width, as a function of diameter/side length for rectangular and circular transducers.

A dual-mode transmitting transducer require a wide pressure wave in order to reach the receiving transducers, as shown in Figure 4.7. A simple geometric consideration of the main-lobe width required to engulf an equally sized transducer placed in the same plane, is shown in Figure 5.3. The red areas indicates the combination of bolus thickness and main lobe width which allow the receiving transducer to not be placed on top of the transmitter, while still being in the main lobe of the pressure field. The result does not take the near field into account. We can, by comparing Figure 5.2 with Figure 5.3, see that the use of dedicated transducers might be hard to realize.

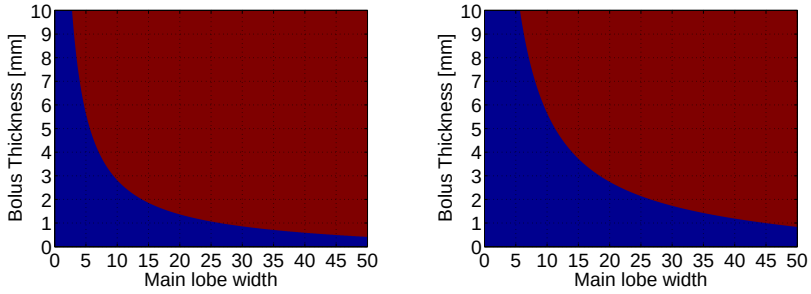

(a) 1 mm diameter / side-length

(b) 2 mm diameter / side-length

(c) 4 mm diameter / side-length

(d) 8 mm diameter / side-length

Figure 5.3: Required main-lobe width/acceptance angle for receiving transducer to be in main lobe of the pressure field. The red area indicate the required combination of main lobe width and bolus thickness.

Let us now look at the data from the experiment work, obtained in accordance with the description found in section 4.5.2. Figure 5.4(a) shows raw data obtained at two different angles with a 8x8 mm transducer, while Figure 5.4(b) show how the preprocessing procedure of section 4.1.1 affects the same measurements in the time domain. The main bang is clearly visible in the raw data, with an amplitude in saturation (0 and 255) near t=0, and a slowly recovering amplitude. The time-gated and Butterworth filtered data has an approximate zero-value amplitude, except for the ultrasonic pulse reflections arriving at

$t = 1e - 5$ and 2e-5, respectively. Also note the change in pulse shape between the two different measurements. The blue line pulse for angle 0° has a larger amplitude and shorter duration compared to the red line pulse for angle 3.4°. In Figure 5.4, the frequency content, here represented by the magnitude of the Fourier transform, of the same zero degree measurement, is shown both before and after preprocessing.

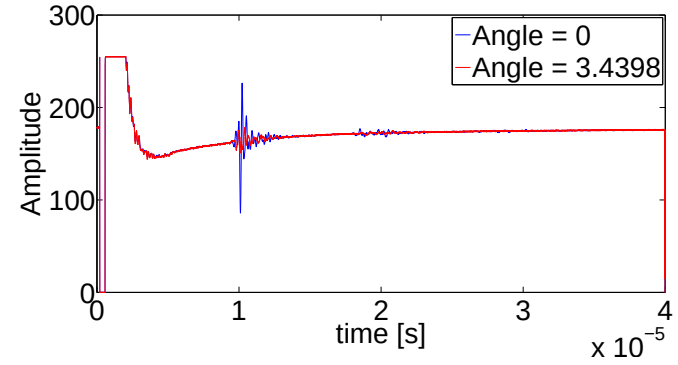

(a)

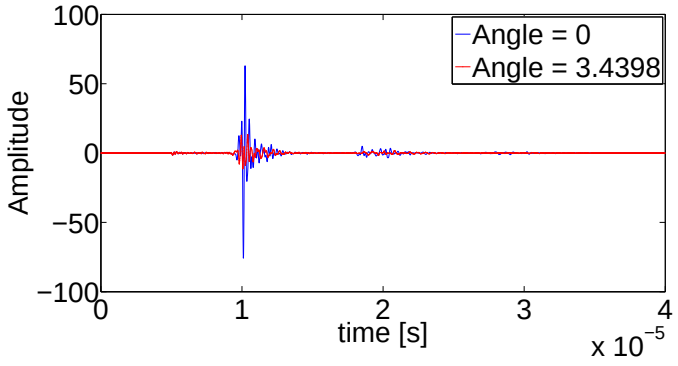

(b)

Figure 5.4: (a):Raw data obtained with 8x8 mm rectangular transducer at two angles. (b): Data after butterworth filtration and time gating.

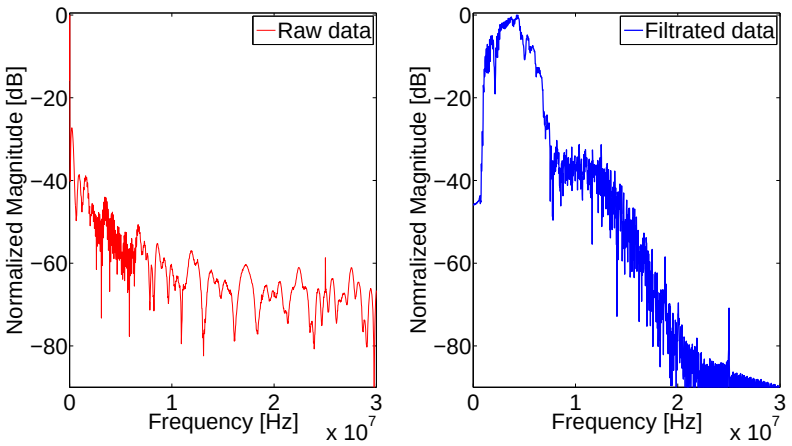

Figure 5.5: Magnitude frequency spectrum of data obtained with 8x8 rectangular transducer at 0 degrees in transducer plane and perpendicular to reflecting acrylic wall. Left: Frequency spectrum of raw data. Right: Frequency spectrum of filtrated and time-gated data.

The main lobe width is defined in this thesis as the angle where the power has dropped to 50%, or -3 [dB], compared to its maximum. The power in each obtained reflection was therefore calculated to find the angle at which this occurs. Figure 5.6 shows the obtained normalized reflection power for both the 4 mm and 8 mm rectangular transducers. As the figure indicates, we are only able to obtain a relatively low angular resolution. Linear interpolation was therefore applied between each measurement angle in all data sets to estimate the main lobe width.

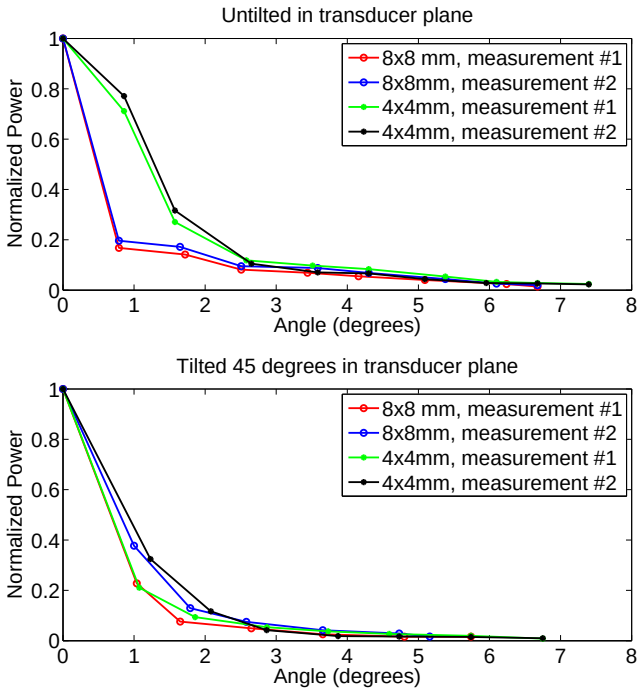

Figure 5.6: Normalized recieved puls power plotted against angle between reflecting layer and transducer plane for 8x8 mm and 4x4 mm rectangular transducer.

It is also worth noticing that there is a difference in measured angles between the data sets, which origin can be found in Table 5.4 and Table 5.5, where the influence of small deviations in hight alteration between data sets on the measurement angle, is shown. The difference in maximum measured angle between the circular and rectangular transducer is because of the size of the PCB containing the circular transducer (see Figure 4.6), which prohibits measurements being acquired at angles above approximately 4 degrees with the experimental equipment used.

Data set number	Side 1 distance [mm]	Side 2 distance [mm]	diff [mm]	Calculated angle [Deg]
1	-	-	0	0
	24.4	23.79	0.61	0.44
	25.25	23.00	1.75	1.25
	25.70	22.32	3.38	2.42
	26.16	21.91	4.25	3.04
	26.42	21.43	4.99	3.57
	26.70	20.98	5.72	4.09
	26.80	20.68	6.12	4.38
2	-	-	0	0
	24.24	23.89	0.35	0.25
	24.71	23.00	1.71	1.23
	25.26	22.5	2.76	1.98
	25.76	21.81	3.95	2.83
	26.26	21.56	4.70	3.36
	26.49	21.07	5.42	3.88

Table 5.4: Measurements for all circular transducers, obtained by caliper ruler, to determine the angle between the transducer plane (front side of water bolus) and the reflecting surface (backside of water bolus). The bolus thickness was kept constant at 15 mm.

Data set number	Side 1 distance [mm]	Side 2 distance [mm]	diff [mm]	Calculated angle [Deg]
1	-	-	0	0
	58.95	57.50	1.45	1.04
	59.50	57.20	2.30	1.65
	60.20	56.50	3.7	2.65
	61.00	55.90	5.1	3.65
	61.91	55.21	6.7	4.79
	62.78	54.78	8.0	5.71
2	-	-	0	0
	59.00	57.60	1.4	1.00
	59.50	57.00	2.5	1.79
	60.10	56.50	3.6	2.58
	61.00	55.90	5.1	3.65
	61.70	55.10	6.6	4.72
	62.10	54.90	7.2	5.14

Table 5.5: Measurements for the 8x8 mm rectangular transducer, obtained by caliper ruler, to determine the angle between the transducer plane (front side of water bolus) and the reflecting surface (backside of water bolus). The bolus thickness was kept constant at 15 mm.

The resulting main beam width is shown in Figure 5.7. The observed center frequency of the transducers was used to find the theoretical line, in the same manner as in Figure 5.2, by using equation 2.62. The error-bars were calculated using the observed bandwidth. The 1 mm transducers does not cross the -3 dB threshold for the applied angles, and the largest measured angle is therefore used.

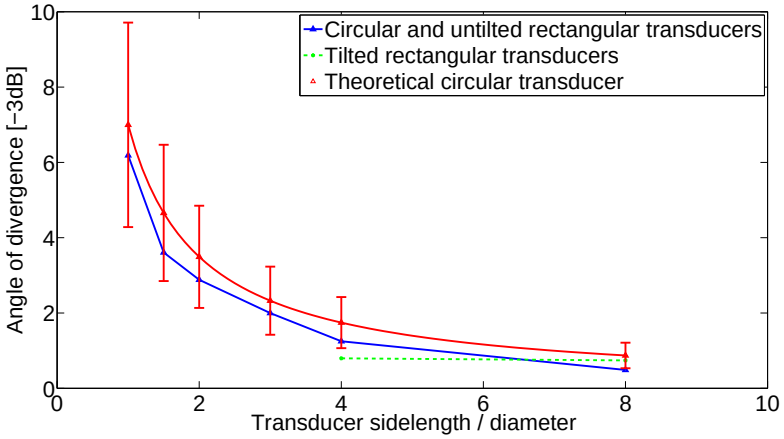

Figure 5.7: Sound pressure half angle for all transducers. The 4 mm and 8 mm transducers are the only ones with a rectangular shape.

5.3 Transducer size and detection

As it is explained in the procedure for this experiment, found in section 4.5.3, the water pressure inside the bolus needed some time to reach equilibrium after moving the linear actuator. The resulting pressure on the transducer mount led to a time lap before the transducer was at the correct distance. Consequently, a test to determine the appropriate time delay between movement of the transducer mount and acquiring data was performed. The measurements shown in Figure 5.8 was obtained by moving the transducer mount 0.5 mm closer to the reflecting wall, and measuring every second for 300 seconds. Data was obtained with a circular transducer with a diameter of 3 mm. As the measurements indicate a constant movement towards the water bolus, this effect is assumed not to be due to a lack of repeatability in the transducer. These findings resulted in each movement of the linear actuator being followed by a delay of 30 seconds to let the water pressure inside the bolus equalize, and thus reducing the pressure on the transducer mount.

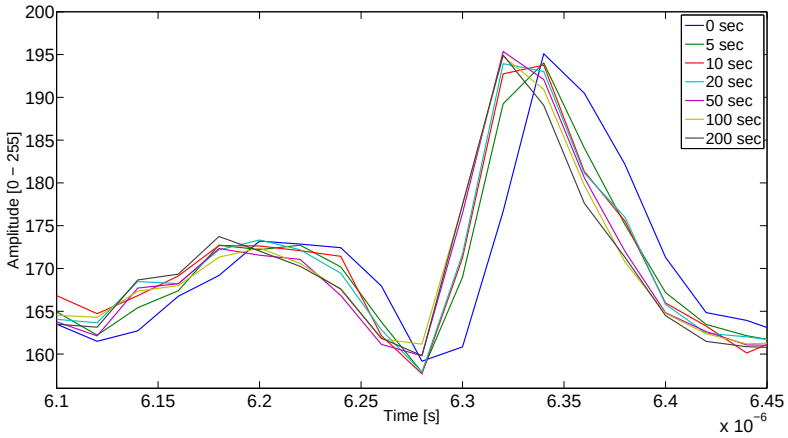

Figure 5.8: Enlarged first reflection. Data obtained after movement of transducer mount and sequential measurements at time instances shown in the figures legend.

The energy envelope detection method used does not always manage to distinguish a signal from the noise. In Table 5.6, the number of detected reflections for a given transducer diameter is given at each distance. An ideal reflecting surface, in this case Acrylic glass, results in detectable reflections at all distances for transducer size of 1.5 mm and up. For the 1 mm transducers, some distances suffered a lower detection rate. When phantom tissue is introduced, detection fails for 1 mm and 1.5 mm diameter transducers for all water bolus thicknesses above 7 mm. Note that during the experiment, with multiple compressions and

expansions of the water bolus, we observed a decreased signal power in the reflected pulse. For the 2 and 3 mm diameter transducers, the observed detection rates were 100 % for all distances.

Transducer diameter [mm] →		3	2	1.5	1
Reflecting layer	Distance [mm]↓				
Acrylic glass plate	10	10	10	10	10
	9.5	10	10	10	10
	9	10	10	10	8
	8.5	10	10	10	9
	8	10	10	10	6
	7.5	10	10	10	10
	7	10	10	10	9
	6.5	10	10	10	10
	6	10	10	10	10
	5.5	10	10	10	10
	5	10	10	10	10
	4.5	10	10	10	10
	4	10	10	10	10
Agar Phantom	10	10	10	0	0
	9.5	10	10	0	0
	9	10	10	0	0
	8.5	10	10	0	0
	8	10	10	0	0
	7.5	10	10	0	0
	7	10	10	1	2
	6.5	10	10	2	1
	6	10	10	2	2
	5.5	10	10	2	3
	5	10	10	4	4
	4.5	10	10	5	5
	4	10	10	5	9

Table 5.6: Number of detected signals for all transducer sizes

The SNR after preprocessing is found in Table 5.7, using equation (4.6) found in section 4.1.2.

In Figure 5.9 and Figure 5.10, the output from the energy envelope method at each distance is shown for the 3 mm and 1.5 mm transducer, respectively. This illustrates the relatively large difference in obtained signal power between transducer sizes.

Transducer Size [mm] / Distance [mm]	3	2	1.5	1
10	44.56	25.03	NA	NA
9.5	45.02	25.80	NA	NA
9	45.53	26.84	NA	NA
8.5	46.28	27.64	NA	NA
8	46.82	29.17	NA	NA
7.5	47.89	29.87	NA	NA
7	48.47	31.06	7.66*	10.88*
6.5	49.48	32.09	13.58*	11.16*
6	50.75	33.34	20.85*	11.06*
5.5	51.69	33.92	27.65*	11.31*
5	57.22	38.97	23.58*	10.98*
4.5	57.12	38.51	25.34	12.38
4	56.20	39.08	28.91	12.16

Table 5.7: SNR found after pre-processing for measurements obtained with phantom tissue. Star (*) indicate SNR based on few detections (4 or less).

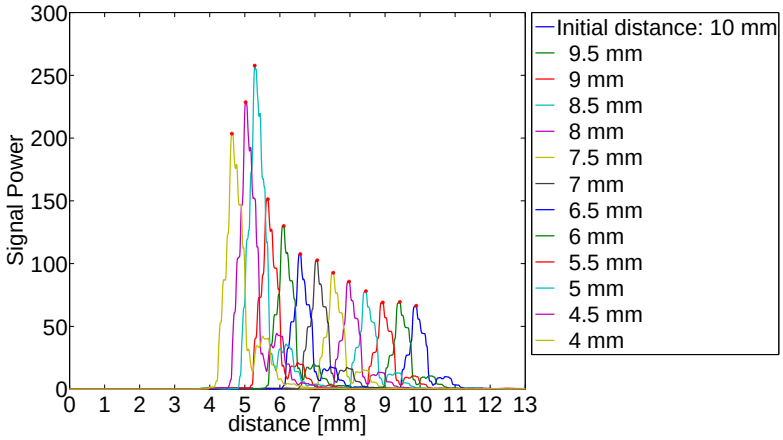

Figure 5.9: Output of energy envelope detection algorithm for 3 mm diameter transducer with phantom material as reflecting wall. Red stars indicate the measured distance.

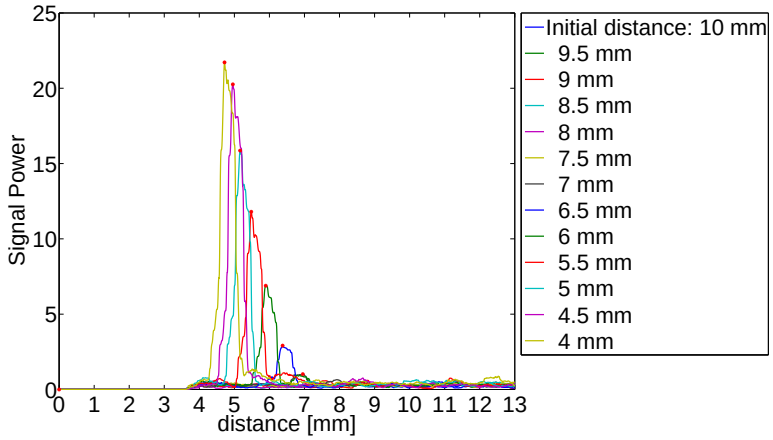

Figure 5.10: Output of energy envelope detection algorithm for 1.5 mm diameter transducer with phantom material as reflecting wall. Red stars indicate the measured distance.

Figure 5.11 and Figure 5.12 shows the found distance compared to the defined *actual* distance for all transducer sizes when Acrylig glass plate and phantom tissue is used as reflecting wall, respectively. A large decrease in accuracy is observed for the 1 mm and 1.5 mm transducers when the phantom tissue is introduced.

The slope of the results found in Figure 5.11 and Figure 5.12 (red lines), are dependent on the calculated sound speed, and have a gradient which is below the blue 1:1 line. We know that the linear actuator moves the transducer mount 0.5 mm between each measurement with a high precision. To look at the possibility of the low gradients being a consequence of an inaccurate sound speed, we first must make the assumption that the results shown in Figure 5.11(b) - (d), at distances above 6 mm, has not been affected by the pressure from the bolus on the transducer mount. If this assumption is valid, the relative distance between two of these measuring points should be constant, regardless of sound speed. Based on this, an attempt to parameterize the dependence the slopes have on sound speed is done by introducing a parameter κ_i, written as

$$\kappa_i = \frac{\sigma_{\Delta d}}{\mu_{\Delta d}},$$

where $\mu_{\Delta d}$ is the mean distance between two measurement points, $\sigma_{\Delta d}$ is the standard deviation of the relative distances, and i indicate the transducer size. A value of $\kappa << 1$ is then an indication that the low gradient is due to sound speed error. The results are found to be $\kappa_3 = 0.03$, $\kappa_2 = 0.0434$ and $\kappa_{1.5} = 0.0270$.

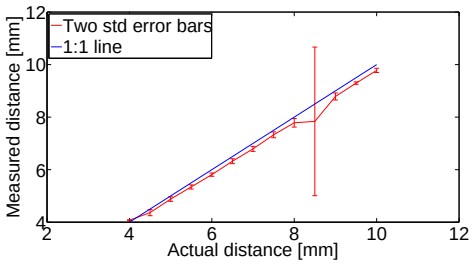

(a) 1 mm transducer. Acrylic glass.

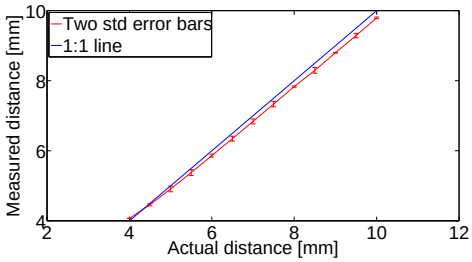

(b) 1.5 mm transducer. Acrylic glass.

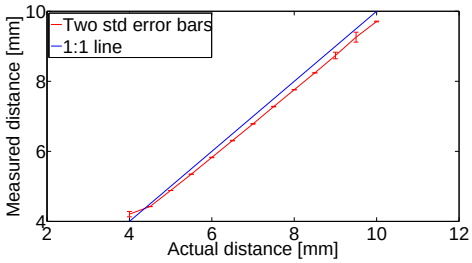

(c) 2 mm transducer. Acrylic glass.

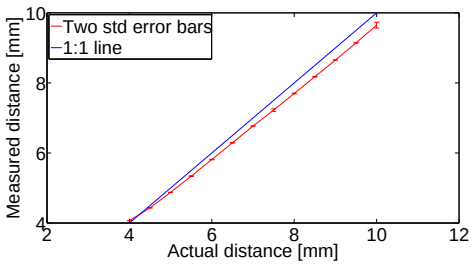

(d) 3 mm transducer. Acrylic glass.

Figure 5.11: Actual distance measurement, obtained with electronic caliper ruler vs. measured distance obtained with transducer, using acrylic glass as reflecting wall.

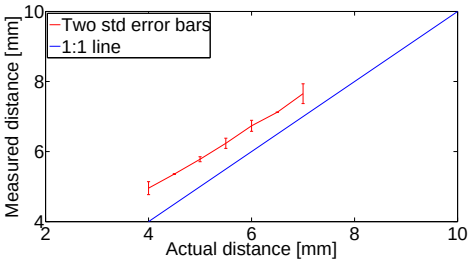

(a) 1 mm transducer. Phantom.

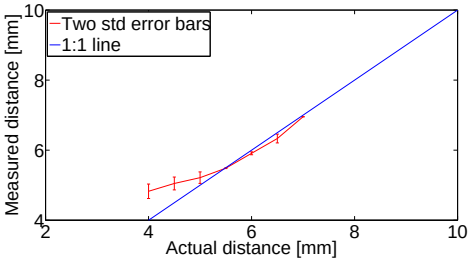

(b) 1.5 mm transducer. Phantom.

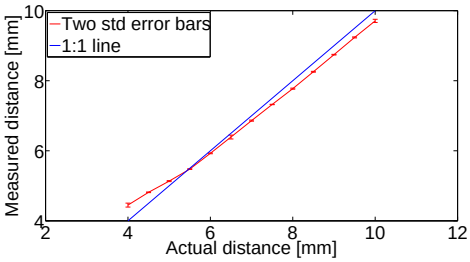

(c) 2 mm transducer. Phantom.

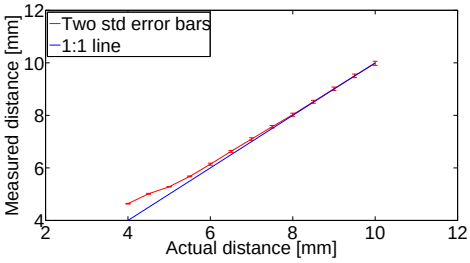

(d) 3 mm transducer. Phantom.

Figure 5.12: Actual distance measurement, obtained with electronic caliper ruler vs. measured distance obtained with transducers, using Agar phantom as reflecting wall.

5.4 In vivo

The following results were obtained by measuring the bolus thickness when it was placed on a human stomach, with different size transducers. Figure 5.13 shows multiple raw data acquisitions with transducer size and shape as denoted in the figure caption. Reflections were not detected with transducers smaller than 2 mm, and is therefore not included. The red line in Figure 5.13(c), was obtained after deliberately altering the angle between transducer and skin surface.

Figure 5.14 shows the processing steps on selected reflections from each transducer size. The measurements shown in column 1 and 2 have been normalized. As the bolus thickness is unknown, accuracy in the found results can only be based on other experiments. The top row indicate that detection is possible with a 2 mm transducer, although the raw signal pulse is hard to identify visually. The 4 mm square transducer gives a notable larger reflection than the circular transducers.

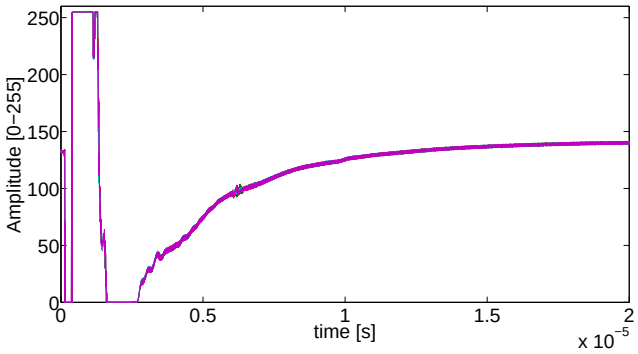

(a) 2 mm

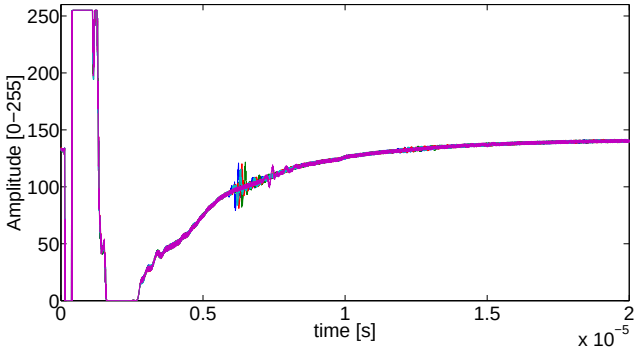

(b) 3 mm

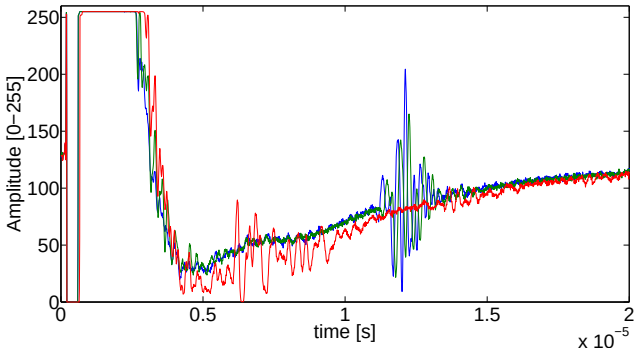

(c) 4 mm

Figure 5.13: In vivo measurements. (a): 2 mm diameter circular transducer. (b): 3 mm diameter circular transducer. (c): 4x4 mm rectangular transducer.

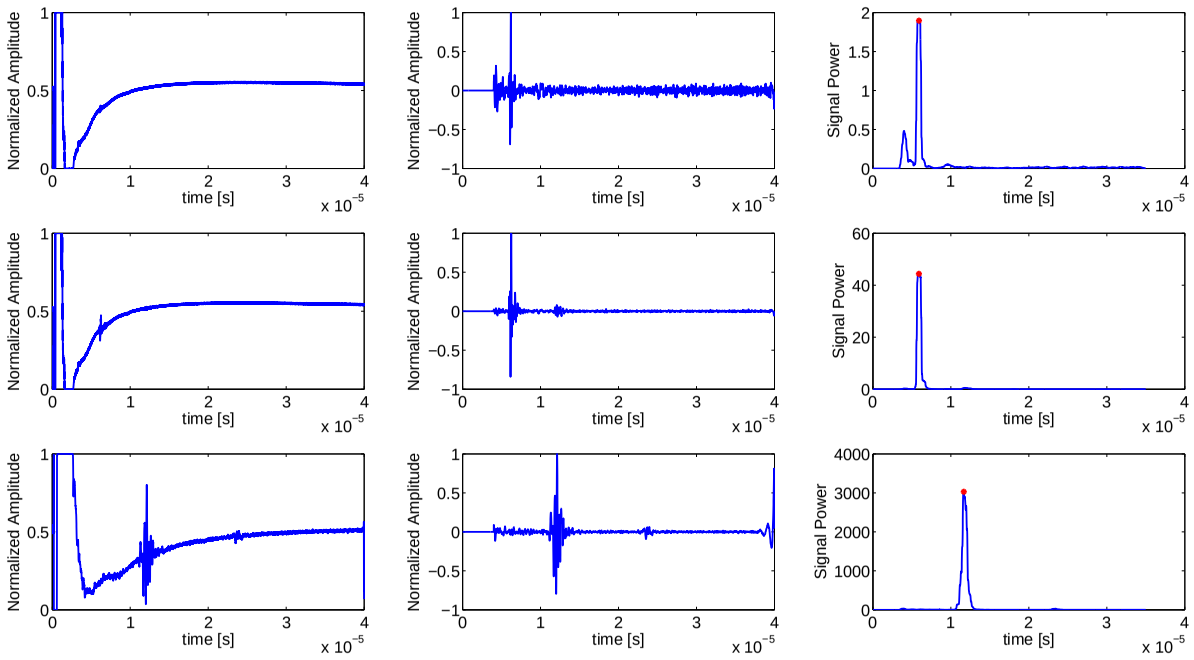

Figure 5.14: Results of in vivo experiment. Top row: Data obtained with 2mm diameter transducer. Middle row: Data obtained with 3 mm diameter transducer. Bottom row: Data obtained with 4 mm square transducer. Left column: Normalized raw data. Middle column: Normalized filtrated and time gated data. Right row: Signal power. Stars indicate detection point.

Chapter 6

Discussion

6.1 Transducer design

The two main concerns regarding transducers shape and size are the amount of received power and the main lobe width, or angle of divergence[1]. The presented theory and experimental results both show that these two parameters are related to the transducer surface size as a trade-off where an improvement in divergence angle result in a reduction in received power, and vice versa.

6.1.1 Main lobe width

Several transducer positioning schemes with multiple dedicated transducers where suggested in section 4.4. In a configuration with multiple transducers placed in close proximity, rectangular transducers would be preferable to circular transducers as they would utilize a larger portion of the available surface area, resulting in more emitted energy. Results shown in Figure 5.7 indicate that the achieved divergence angles are too small for such configurations, purely from the geometric limitation of placing the transmitting and receiving transducers directly side-by-side. There are however cases where such a design could work, e.g. by increasing the minimum bolus thickness so the beam is allowed to spread over a longer distance. As an increased bolus thickness implies higher absorption of both ultrasonic pulses and microwave energy, this solution would not be suitable for our application. An alternative approach is a decrease in the ultrasound transducer surface area, but this would unfortunately lead to a reduction in received power, as also discussed later in this thesis. Another option for allowing multiple dedicated transducers could be to increase the center frequency

[1] Angle of divergence used interchangeably with main lobe width and sound pressure half angle in the literature. Must not be confused with frequency divergence.

of the transducers, and consequently in the transmitted pulse, which will lead to greater divergence. Higher frequency transducers has been developed [46], but has not been subject of investigation due to the known fact that signal attenuation is proportional to the frequency squared. In addition, this would mean that the near field length would increase which counteracts geometric gain obtained from an frequency increase. Using multiple dedicated transducers are for these reasons considered impractical for our medical application.

Using transducers in single mode favores circular transducers, as they do not have any geometric discontinuities resulting in low angular divergence. The low divergence around the corners of rectangular transducers are not clearly visible in the experimental results of Figure 5.7. This is probably due to the relatively small achieved angular resolution in combination with difference in measurement angles between data-sets, as shown in Table 5.4, as the linear interpolation used to find the -3 dB drop does not compensate for this. A small drop in beam width is detected for 4 mm square transducer when the transducer was tilted 45 degrees relative to the angular change of the plane, while the 8 mm transducer has to low divergence angle for this to be detected. These results clearly shows that circular shaped PVDF transducers are more robust with respect to beam geometry.

The need for a minimum main lobe width is however still present for practical reasons, due to the possibility of the patient skin surface and the transducer plane not being parallel. The in vivo experiment offered some experience in obtaining ultrasound measurements in a situation similar to that of VUR hyperthermia treatment. A rough estimate of a minimum acceptable divergence angle is thought to be in the range of 2-3 degrees based on the difficulty to obtain a reflected pulse when the in vivo experiment was conducted. It should also be noted that as the water bolus is compressed, positioning the transducer in parallel with subjects skin gets easier, which suggests that the requirements on divergence angle lessens for decreasing bolus thickness. This in turn affects the requirements on maximum near field length. According to the theoretical near field length as a function of transducer diameter and frequency, shown in Figure 4.3, a transducer diameter of 2.5 mm corresponds to a near field length in the range of 5 mm, dependent on frequency, which should be sufficient.

6.1.2 Signal power and SNR

The most interesting information regarding received signal power is found when the tissue phantom was introduced in the detection experiment found in section 5.3. Comparing Figure 5.9 with Figure 5.10 shows us that the reflected signal power from a skin like surface is simply to low for the 1 mm and 1.5 mm circular transducer, which points to a minimum transducer size of 2 mm.

The expected influence of a reduction in water bolus thickness is a steady increase in the received signal power, and thus the SNR. This pattern is found

for all transducer sizes except the 3 mm, which experiences a slight reduction for bolus thickness of 4.5 and 5 mm (see Figure 5.9). The explanation is found in the experimental set-up. As the thickness lessens, the water inside the bolus exerts an increased force on the transducer mount causing it to bend, as also mentioned in section 4.5.3. Smaller size transducers have a relatively wide main beam and short near field length which leads to this effect being practically negligible. Longer near field length in combination with a narrow beam leaves the small SNR reduction for the 3 mm transducer logical. In addition to the geometric aspect of the reflected wave missing the transducer, an increase in destructive interference between incident and reflected wave might contribute to the observed SNR reduction.

An effect observed for all transducer sizes is that gain values ¿ 63 result in large oscillations throughout the measurement vector. This is probably due to multiple reflection in the poor acoustical backing offered by the microwave antenna.

The manner of making multiple circular transducers with the same PVDF film, explained in section 4.3, can possibly have resulted in an increase of electrical noise, as the top, conducting gold layer's surface area is much larger than the actual transducer apertures. Reducing the size of the PVDF film to match that of the aperture might therefore give a better SNR.

6.2 Detection and accuracy

The detection rate of the implemented energy envelope method has been found to be a 100 % for both the 2 and 3 mm diameter transducers. As reported in Table 5.6 and Table 5.7, the detection rate and SNR falls drastically for further reduction in transducer diameter. To increase the detection rate alterations of the ΔA parameter in the adopted *peakdet* Matlab function was atempted (see section 4.1.2). This led to more detections, but at the cost of an increased false-alarm rate.

Accuracy in the distance measurements are illustrated by the error bars in Figure 5.11 and Figure 5.12. As the number of measurements acquired at each distance is relatively small, bombastic conclusions regarding the exact accuracy of the distance measurements can not be statistically justified. The reason for keeping the data set sizes small is the mechanical nature of the experimental set-up. Obtaining larger data-sets would increase the probability of incomparable results for the different transducer sizes, as the number of compressions and decompressions of the water bolus would increase. That being said, using two standard deviation of the results obtained with 2 and 3 mm transducers as an accuracy measurement, results in an estimated accuracy below 0.1 mm, regardless of reflecting surface.

With the current detection method, the poor detectability for 1 and 1.5 mm

transducers infer that great care must be taken regarding placement on patients skin surface and acoustical contact between transducer and media, if attempted. As already discussed, the SNR values suggests that these transducer sizes are not suitable for the VUR diagnostic system.

The coherence between the ultrasonic distance measurements and the actual distance obtained with a caliper ruler, is at first inspection fairly poor. The gradient of the curves in Figure 5.11 and Figure 5.12 are all below 1 and varies with distance. However, the parameter values of κ, presented at the end of section 5.3, are deemed small enough to assume that the below one gradient comes down to an inaccurate sound speed estimation. To further investigate this deviation from the expected result, we can look at how the sound speed was calculated by using Lubber and Graffs' simplified equation [39]. There are some issues with most sound speed formulas, including this, being intended on distilled water while the water bolus is filled with tap water, but the expected difference from this effect are in all practical matters negligible. A slightly larger error can be expected from water temperature fluctuations as temperature measurements could not be conducted during the four hour data acquisition time. This may have caused the actual sound speed to differ between data sets. In addition, the water bolus contain an open poor filter which might influence the velocity.

As the bolus thickness in Figure 5.11 and Figure 5.12 approaches 4 mm, the measured distance seams to curve from below to above the actual distance. This trend is more distinct for the tissue phantom measurement. A possible reason, observed during data collection, is the elastic nature of the phantom material leading to a compression of the phantom as well as the water bolus, in combination with the pressure on the transducer mount already discussed.

The seemingly lower error when the Agar based phantom tissue was used in the case of 2 and 3 mm transducers at large distances, comes down to the accuracy of initial placement. Programming the linear actuator from Matlab led to data gathering not requiring human interaction, except when changing the type of reflecting surface. The fact of the matter is that the ultrasound measurements are probably more accurate than the mechanical measuring equipment available at the lab, and this particular deviation between phantom tissue and Acrylic glass reflecting surface, probably comes down to caliper ruler resolution and human error.

Improving the detection rate might be achievable by altering the transmitted pulse shape and duration. It has previously been mentioned that a chirp signal might increase the accuracy and detectability. As dedicated transducers have been found unrealizable with the achieved main lobe width, a more thorough investigation into the use of time extended pulses is required. Regardless of pulse shape, transmitting a know pulse opens up the opportunity to implement matched filtering detection methods, which are utilized for their robustness in numerous other applications. As shown in section 4.1.2, the matched filter requires a priori information about the waveform. Since the waveform is convo-

luted with the systems transfer function before being received, the transmitted square pulse can not be used in matched filtration. Extracting the waveform from measurements to use as the a priori waveform was attempted. Compared to the energy envelope method, the variations between obtained reflection lengths and shapes led to an inferior detection accuracy. Matched filtration therefor proved fruitless in these experiments, but is stilled considered as a possible filtration method as it maximizes the SNR.

Estimating the thickness of the skin layer, fat layer and muscle layer was originally thought of as a natural next step. However, integration into the microwave antenna without disturbing its performance to a large extent makes such estimations *very* difficult to achieve. Poor acoustical backing, the small PVDF surface area required for robustness and relatively high frequencies are all factors that diminish the available signal strength. Multi-layer detection has therefor not been attempted.

6.3 Microwave antenna integration

As we have seen, a circular PVDF transducer in single mode, with a size in the range of 2-3 mm looks to be the most feasible for water bolus thickness estimation. It is still a manner of placement on the microwave antenna. Angular difference between skin surface and microwave antenna can be found by using a minimum of three transducers. Although no transducer is placed at the center of the antenna, the angle of the plane, and thus the distance from the center can be calculated. Placement of PVDF elements on the microwave antenna effects the SAR pattern, as described in chapter 3. PCB-board layout of such a prototype is shown in Figure 6.1. The simulations on the effect of PVDF implementation show that the electric leads supplying a ultrasound transducer has a significant impact on the SAR-pattern. Signal leads to each transducer can be introduced at the corners of the DCC-antennas aperture where the 90 degree phase shift between the sides will reduce the interference with the emitted microwave radiation. To suppress the disturbance even further, a use of common electrical ground for both microwave antenna and ultrasound transducer is suggested. Alternatively, a third PCB layer dedicated to ultrasound transmission can be introduced. Since the microwave antenna is designed to work with the current backing, this layer will have to be implemented as a new middle layer.

The PVDF transducer placement shown in Figure 6.1 is outside the radiometric elliptical antenna at the center, which the preliminary work in [10] suggest is needed. Although no research regarding the effect on the microwave antenna of such a placement has been preformed, a decrease in the DCC antennas heating performance can most likely be sorted out by simply increasing the input power. A similar approach for improving the radiometry is not possible as it is a passive devise.

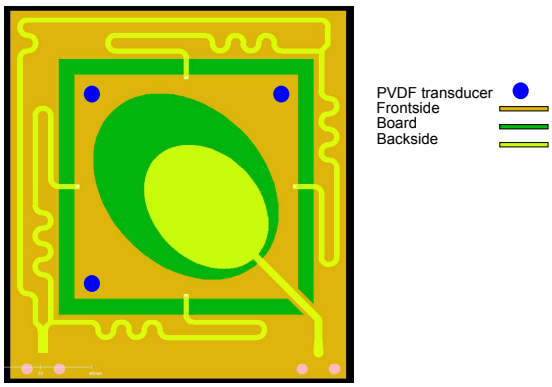

Figure 6.1: Suggested placement of transducers. Transducer surface size is 2.5 mm.

Chapter 7

Conclusion and further work

This study involves experimental work on the feasibility of integrating PVDF ultrasound transducers into a microwave hyperthermia antenna for VUR diagnostics. Real time knowledge of water bolus thickness is vital for improving the diagnostic systems quality assurance. This thesis shows that such thickness measurements can be obtained with PVDF film transducers.

The presented results shows that a circular PVDF ultrasound transducer, with a diameter between 2 and 3 mm, performs best for measuring the water bolus thickness. These sizes are selected due to superior results regarding angle robustness and pulse detectability. Experimental work with phantom tissue gave a minimum SNR, after filtration, of 25.03 and 44.56 for the 2 and 3 mm transducer, respectively. The 3 mm transducer's superior SNR comes at the cost of a long near field and narrow main beam. As a compromise, a 2.5 mm transducer with a near field length of 5 mm and main beam angle of 4.4 degrees, dependent on frequency, is proposed as the best candidate for prototyping and future development.

Implementing transducers on the microwave heating antennas surface will, to some extent, effect its performance. Preliminary research has shown that the elliptical antenna used for radiometry is the most sensitive, and the suggested placement of transducers is therefor outside its aperture. Future changes in the microwave antenna design will naturally lead to a re-evaluation of the placement. The acoustical backing offered by the microwave antenna is adequate, but has shown to limit the possibility of increased gain.

Further work could involve thorough mapping of the effect of suggested transducer placement on the microwave antenna, and optimization of the SNR through pulse design together with testing of alternative detection algorithms. If accept-

able results are acquired, software for incorporating the ultrasound readings into the diagnostic system has to be developed.

Bibliography

[1] S. K. Jacobsen Ø. Klemetsen, Y. Birkelund. Design of medical radiometer front-end for improved performance. *Progress In Electromagnetic Research B*, 27:289–306, 2011.

[2] J. Molittierno A. Kirch, J. Grattan-Smith. The role of magnetic resonance imaging in pediatric urlology. *Curr. Opin. Urol*, 16:283–90, 2006.

[3] G. Andria, F. Attivissimo, and N. Giaquinto. Digital signal processing techniques for accurate ultrasonic sensor measurement. *Measurement*, 30(2):105–114, 2001.

[4] K. Arunachalam, P. Maccarini, V. DeLuca, P. Tognolatti, F. Bardati, B. Snow, and P. Stauffer. Detection of vesicoureteral reflux using microwave radiometry: System characterization with tissue phantoms. *Biomedical Engineering, IEEE Transactions on*, (99):1–1, 2011.

[5] M. B. Taylor B. W. Snow. Non-invasive vesicoureteral reflux imaging. *Journal of Pediatric Urology Company*, 6:543–9, 2010.

[6] R. R. Bailey. An overview of reflux nephropathy. *Reflux Nephropathy*, pages 3–13, 1979.

[7] C.A. Balanis. *Antenna theory: analysis and design*. Harper & Row New York, 1982.

[8] John P. Bentley. *Principles of Measurement Systems*. Pearson Education Limited, fourth edition, 2005.

[9] Y. Birkelund, O. Klemetsen, S. Jacobsen, K. Arunachalam, P. Maccarini, and P. Stauffer. Vesicouretal reflux in children: A phantom study of microwave heating and radiometric thermometry of pediatric bladder. *Biomedical Engineering, IEEE Transactions on*, (99):1–1, 2011.

[10] Y. Birkelund and F. Melandsø. Integrated ultrasound sensor for microwave heating and radiometry in medical applications. 2011.

[11] David T. Blackstock. *Fundamentals of physical acoustics*. John Wiley & Sons, Inc., 2000.

[12] Sindre Holsbøe Brelum. A numerical study of planar elliptical antennas applied to ultrawideband (uwb) imaging of breast tissue. Msc thesis, University of Tromsø, August 2008.

[13] S. Buckingham and D. Sattelle. Fast, automated measurement of nematode swimming (thrashing) without morphometry. *BMC neuroscience*, 10(1):84, 2009.

[14] S.N. Rosen D. P. Frush, L.F. Donnelly. Computed tomography and radiation risks: what pediatric health care providers should know. *Pediatrics*, 112:951–7, 2003.

[15] K Darge and H Riedmiller. Current status of versicoureteral reflux diagnosis. *World Journal Urology*, 22:88–95, 2004.

[16] Eric J. Hall Walter E. Berdon David J. Brenner, Carl D. Elliston. Estimated risks of radiation-induced fatal cancer from pediatric ct. *Am J. Roentgenol*, 176:289–96, 2001.

[17] F. A. Duck. *Physical properties of tissue*. Academic Press Limited, 1990.

[18] P. Reddy C. Sheldon E. Minevich E. Traxel, W. DeFoor. Risk factors for urinary tract infections after dextranomer/hyaluronic acid endoscopic injection. *J. Urol*, 182:1708–13, 2009.

[19] J. A. Gallego-Juárez. Piezoelectric ceramics and ultrasonic transducers. *Scientific Instruments*, 22:804–816, 1989.

[20] World Precision Instruments. http://www.wpiinc.com/index.php/4898.html. web page, 2011.

[21] R. Issels. Hyperthermia combined with chemotherapy–biological rationale, clinical application, and treatment results. *Onkologie*, 22(5):374–381, 1999.

[22] N. Cheek J. David. *Fundamentals and Applications of Ultrasonic Waves*. CRC Press, 2002.

[23] S. Jacobsen, P.R. Stauffer, and D.G. Neuman. Dual-mode antenna design for microwave heating and noninvasive thermometry of superficial tissue disease. *Biomedical Engineering, IEEE Transactions on*, 47(11):1500–1509, 2000.

[24] Mark A. Yoder James H. McClellan, Ronald W. Schafer. *Signal Processing First*. Pearson Education Limited, 2003.

[25] C.R. Hill J.C. Bamber. Ultrasonic attenuation and propagation speed in mammalian tissues as a function of temperature. *Ultrasound Med. Bio.*, 5:149–157, 1979.

[26] J.R. Jensen. *Remote sensing of the environment*. Pearson Education India, 2009.

[27] J. Rivenez J.Marini. Acoustic fields from rectangular ultrasonic transducers for non-destructive testing and medical diagnosis. *Ultrasonics*, pages 251–256, nov. 1974.

[28] J. Trieger K. Darge. Vesicoureteral reflux grading in contrast-enhanced voiding urosonography. *Eur. J Radiol.*, 43:122–8, 2002.

[29] M W Vogel R Niessner K Zell, J I Sperl and C Haisch. Acoustical properties of selected tissue phantom materials for ultrasound imaging. *Phys. Med. Biol.*, 52:475–484, 2007.

[30] Valeria De Luca Fernando Bardati Brent W Snow Paul R stauffer Kavita Arunachalam, Paolo F Maccarini. Modeling the detectability of vesicoureteral reflux using microwave radiometry. *Physics in medicine and biologi*, 55:5417–5435, 2010.

[31] Leon A. Frizzell Kenneth B. Ocheltree. Sound filed calculation for rectangular sources. *IEEE Transaction on ultrasonics, and frequency control*, 36:242–248, 1989.

[32] J. Keshvari, R. Keshvari, and S. Lang. The effect of increase in dielectric values on specific absorption rate (sar) in eye and head tissues following 900, 1800 and 2450 mhz radio frequency (rf) exposure. *Physics in Medicine and Biology*, 51:1463, 2006.

[33] J.C. Kumaradas and M.D. Sherar. Optimization of a beam shaping bolus for superficial microwave hyperthermia waveguide applicators using a finite element method. *Physics in medicine and biology*, 48:1, 2003.

[34] JJW Lagendijk. Hyperthermia treatment planning. *Physics in medicine and biology*, 45:R61, 2000.

[35] S. Marild U. Joal M. Hellstrom, B. Jacobsen. Voiding cystourethrography of reflux nephropathy in children with urinary tract infection. *Am. J. Roentgenol*, 22:801–4, 1989.

[36] P. Tewari R.S. Singh M. O. Culjat, D. Goldenberg. A review of tissue substitutes for ultrasound imaging. *Ultrasound in Med. & Biol.*, 36:861–873, 2010.

[37] D. Marioli, C. Narduzzi, C. Offelli, D. Petri, E. Sardini, and A. Taroni. Digital time of flight measurement for ultrasonic sensors. In *Instrumentation and Measurement Technology Conference, 1991. IMTC-91. Conference Record., 8th IEEE*, pages 198–201. IEEE, 1991.

[38] L. Medina, E. Moreno, G. González, and L. Leija. Circular ultrasonic transducer characterization: theoretical and experimental results. *Revista mexicana de física*, 49(006), 2009.

[39] NPL. http://resource.npl.co.uk/acoustics/techguides/soundpurewater/speedpw.pdf. web page, 2000.

[40] J. Overgaard, SM Bentzen, D. Gonzalez Gonzalez, M. Hulshof, G. Arcangeli, O. Dahl, and O. Mella. Randomised trial of hyperthermia as adjuvant to radiotherapy for recurrent or metastatic malignant melanoma. *The Lancet*, 345(8949):540–543, 1995.

[41] PiezoTech. http://www.piezotech.fr/. web page, 2011.

[42] D.M. Pozar. *Microwave engineering*. Wiley-India, 2005.

[43] S. Ganguly S. Banik, S. Bandyopadahyay. Bioeffects of microwave - a brief review. *Bioresource Technology*, 87:155–159, 2003.

[44] R.C. Sanders and T.C. Winter. *Clinical sonography: a practical guide*. Lippincott Williams & Wilkins, 2006.

[45] Louis L. Scharf. *Statistical Signal Processing: Detection, Estimation and Time Series Analysis*. Addison-Wesley Publishing company, 1991.

[46] MD Sherar and FS Foster. The design and fabrication of high frequency poly (vinylidene fluoride) transducers. *Ultrasonic imaging*, 11(2):75–94, 1989.

[47] BW Snow, K. Arunachalam, V. De Luca, PF Maccarini, Ø. Klemetsen, Y. Birkelund, TJ Pysher, and PR Stauffer. Non-invasive vesicoureteral reflux detection: Heating risk studies for a new device. *Journal of Pediatric Urology*, 2011.

[48] Measurement Specialties. http://www.meas-spec.com/product. web page, 1. december 2011.

[49] Measurement Specialties. Piezo film sensors. Technical report, Measurement specialties, Inc. Sensor products division, April 1999.

[50] T. Sugahara, J. Van Der Zee, H.H. Kampinga, Z. Vujaskovic, M. Kondo, T. Ohnishi, G. Li, H.J. Park, D.B. Leeper, V. Ostapenko, et al. Kadota fund international forum 2004. application of thermal stress for the improvement of health, 15–18 june 2004, awaji yumebutai international conference center, awaji island, hyogo, japan. final report. *International journal of hyperthermia: the official journal of European Society for Hyperthermic Oncology, North American Hyperthermia Group*, 24(2):123, 2008.

[51] G. Turin. An introduction to matched filters. *Information Theory, IRE Transactions on*, 6(3):311–329, 1960.

[52] Perre Ueberschlag. Pvdf peiezoelectric polymer. *Sensor Review*, 21:118–125, 2001.

[53] H.R. Underwood, A.F. Peterson, and R.L. Magin. Electric-field distribution near rectangular microstrip radiators for hyperthermia heating: Theory versus experiment in water. *Biomedical Engineering, IEEE Transactions on*, 39(2):146–153, 1992.

[54] J. S. Nunes S. Lanceros-Mendez G. Minas V. F. Cardoso, J. G.Rocha. Piezoelectric beta-pvdf polymer films as fluid acoustic microagitator. In *IEEE Symp. Industrial Electronics, Cambridge, MA*, July 2008.

[55] ML Van der Gaag, M. De Bruijne, T. Samaras, J. Van der Zee, and GC Van Rhoon. Development of a guideline for the water bolus temperature in superficial hyperthermia. *International journal of hyperthermia*, 22(8):637–656, 2006.

[56] GC Van Rhoon, PJM Rietveld, and J. Van der Zee. A 433 mhz lucite cone waveguide applicator for superficial hyperthermia. *International journal of hyperthermia*, 14(1):13–27, 1998.

[57] R.C. Waag. A review of tissue characterization from ultrasonic scattering. *Biomedical Engineering, IEEE Transactions on*, (12):884–893, 1984.

[58] T.T. Wilheit. A review of applications of microwave radiometry to oceanography. *Boundary-Layer Meteorology*, 13(1):277–293, 1978.

[59] Moore Workman, Kishoni. *Ultrasonic Testing*. American Society for Nondestructing Testing, 2007.

[60] Kavitha Arunachalam Paolo Maccarini Paul R Stauffer Yngve Birkelund, Svein Jacobsen. Flow patterns and heat convection in a rectangular water bolus for use in superficial hyperthermia. *Phys. Med. Biol.*, 54:3937–3953, 2009.

Appendix A

Factors relating beam width with transducer size

Factors related to beam width of ultrasonic piston oscillators (circular and rectangular)

dB-drop free-field	dB-drop echo mode	amplitude ratio p/p_0	factor k_{disk}	factor $k_{rectangle}$	valid for distances > x $D^2/4\lambda$ resp. > x $A^2/4\lambda$ resp. > x $B^2/4\lambda$
0	0	1.00000	0	0	0.8
0.5	1.0	0.94406	0,21497	0.18599	0.8
1.0	2.0	0.89125	0.30254	0.26150	0.9
1.5	3.0	0.84140	0.36872	0.31839	0.9
2.0	4.0	0.79433	0.42365	0.36547	1.0
2.5	5.0	0.74989	0.47129	0.40616	1.1
3.0	6.0	0.70795	0.51367	0.44224	1.2
3.5	7.0	0.66834	0.55200	0.47477	1.3
4.0	8.0	0.63096	0.58708	0.50444	1.4
4.5	9.0	0.59566	0.61947	0.53173	1.5
5.0	10.0	0.56234	0.64956	0.55699	1.6
6.0	12.0	0.50119	0.70403	0.60248	1.8
7.0	14.0	0.44668	0.75226	0.64244	2.0
8.0	16.0	0.39811	0.79539	0.67790	2.2
9.0	18.0	0.35481	0.83425	0.70958	2.4
10.0	20.0	0.31623	0.86943	0.73803	2.6
12.0	24.0	0.25119	0.93050	0.78678	3.0
20.0	40.0	0.10000	1.09000	0.91000	4.4
∞	∞	0	1.21967	1.00000	∞

Appendix B

List of figures

List of Figures

Appendix C

List of tables

List of Tables


UNIVERSITY
OF TROMSØ